

Electromagnetic simulations for the He6-CRES RF system

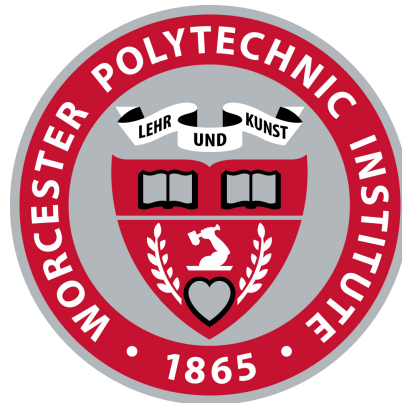
A Major Qualifying Project Report
submitted to the Faculty of the
WORCESTER POLYTECHNIC INSTITUTE
in partial fulfillment of the requirements for the
Degree of Bachelor of Science

by
Luciano Malavasi

Advisors:
Dr. David Medich
Professor of Physics

Dr. Sergey Makaroff
Professor of Electrical & Computer Engineering

Dr. Alejandro García
Professor of Physics, University of Washington



This report represents the work of one or more WPI undergraduate students submitted to the faculty as evidence of completion of a degree requirement. WPI routinely publishes these reports on its website without editorial or peer review.

Abstract

The sensitivity of the He6-CRES experiment is limited by frequency-dependent oscillations in the signal-to-noise ratio (SNR) observed in initial data. We model these oscillations as a result of various reflective components in the apparatus forming a multi-mirror Fabry-Pérot cavity. Electromagnetic simulations of key RF components along with a model for the reflections will allow us to mitigate the issue of irregular SNR. Prior work has characterized several elements of our radio-frequency (RF) system in simulation, namely the quarter-wave polarizer and circular-to-rectangular waveguide transition. In this project, we construct a model and simulation of the full He6-CRES waveguide system, including simulating CRES radiation in a decay cell, enabling a more comprehensive computational study of the observed SNR variations.

Acknowledgements

I would like to thank the many individuals without whom this research would not have been as educational, fun, and successful as it was. At WPI, my gratitude goes to the unwavering support of my advisors Dr. David Medich and Dr. Sergey Makaroff, who have both encouraged me to reach for new and exciting opportunities throughout my undergraduate career. At the University of Washington, I would like to thank my PI and research mentor Dr. Alejandro García, and Dr. Nicholas Buzinsky and RJ Taylor for their guidance and many patient explanations. I am grateful to the University of Washington Center for Experimental Nuclear Physics and Astrophysics (CENPA) for being a wonderful environment for physics research and a welcoming community.

I am very grateful for my peers and classmates in WPI, especially Charlie Tribble and Kylar Coleman-Foley who have been a continuous source of adventures and camaraderie in physics since freshman year and my many friends in ECE. I am equally grateful for the deep connections I have made with my REU cohorts at UC Santa Barbara and the University of Washington: their achievements continually inspire me and push me to be a better physicist. Dr. David Stuart and Dr. Patrick Freeman at UC Santa Barbara have not only been my research mentors but also given me so much advice when the future seemed uncertain.

I would like to thank Taimur Khan and Matt McEvoy for brotherhood and direction. My mother and sister who remind me every day of the importance of family. The many other people in my personal and academic life whose profound contributions could not be enumerated here. Finally, my wonderful partner Sycamore Herlihy for the gift of infinite joy, stability, and inspiration.

This research was partially conducted at the University of Washington CENPA over summer 2023 sponsored by the National Science Foundation (NSF) REU grant PHY-2243362.

In memory of my father.

Contents

1	Background	7
1.1	Beta decay experiments and b_{Fierz}	7
1.2	Cyclotron Resonance Emission Spectroscopy	8
1.3	Theory of waveguides	9
1.3.1	Power flow and attenuation in waveguides	11
1.4	He6-CRES waveguide system	11
1.5	RF network parameters	12
1.5.1	Scattering parameters	12
1.5.2	Transfer scattering parameters	13
1.5.3	Generalizing to N -port networks	14
1.5.4	Observed SNR oscillations	15
2	Methods	17
2.1	Simulating individual components	17
2.1.1	Circular-to-linear polarizer	17
2.1.2	Circular-to-rectangular waveguide transition	19
2.1.3	Waveguide termination	20
2.2	Modeling the full waveguide system	20
2.2.1	Defining a CRES source	20
2.2.2	HFSS waveguide model	22
2.2.3	Power delivered to amplifier	22
3	Results	24
3.1	Simulating individual components	24
3.1.1	Circular-to-linear polarizer	24
3.1.2	Circular-to-rectangular waveguide transition	25
3.1.3	Behavior in series	27
3.2	Constructing a simulated CRES source	28
3.2.1	Simulated CRES source power spectrum	28
3.3	Power delivered to LNA	29
4	Discussion	32
4.1	Summary	32
4.2	Outlook	33

A Noise

36

List of Figures

1.1	Feynman diagram of β^- decay	8
1.2	^{83}Kr CRES data from [1]. Right: Spectrogram showing full 1.1 GHz bandwidth. Left: Zoom-in on a single CRES event	9
1.3	Cross section of TE_{10} in a rectangular waveguide (a) and TE_{11} in a circular waveguide, polarized along x (b) [14]	10
1.4	Diagram of He6-CRES system. A : Decay cell. B : Polarizer. C : circular-to-rectangular waveguide transition. D : Rectangular waveguide. E : to LNAs. F : circular waveguide terminator.	12
1.5	2-port S-parameters, with incident and reflected field amplitudes a_n and b_n .	12
1.6	Cascading three 4-port balanced networks with T-parameters [18]	15
1.7	SNR vs. frequency varying magnetic field strength, before installing terminator	16
1.8	SNR vs. frequency varying magnetic field strength, with terminator	16
2.1	Polarizer model in HFSS, with waveguide walls hidden	18
2.2	Circular-to-rectangular waveguide transition model in HFSS	19
2.3	Conical waveguide termination model with backing PEC cap in orange in HFSS	20
2.4	Lattice of points on the surface of a 3mm cube on which the near-field source is defined. Points are spaced by 0.1 mm and colored by index.	21
2.5	Cross section of actual He6-CRES waveguide system (top) compared to HFSS model	22
2.6	Real component of S_z [W/m^2] over the WR42 waveguide cross section, with $y = 0$ integration line traced.	23
3.1	Polarizer S_{11} and S_{21}	24
3.2	Polarizer phase shift along x and y	25
3.3	Polarizer axial ratio	25
3.4	Active S_{21} of RHCP and LHCP waves transmitting to x- and y-polarized mode in the polarizer	26
3.5	Waveguide transition S_{11} and S_{21}	26
3.6	S_{11} of LHCP and RHCP wave through both components in series. HFSS simulation in solid lines, T parameter equivalent in dashed lines	27
3.7	S_{21} of LHCP and RHCP wave through both components in series. HFSS simulation in solid lines, T parameter equivalent in dashed lines	28
3.8	E-field radiated from a simulated CRES source with cube source geometry at 18 GHz	29

3.9	Power spectrum of the CRES source delivered to the rectangular waveguides in either direction (red: port 1, blue: port 2) and total power (orange)	30
3.10	Power flow in the rectangular waveguide waveguide [fW] at LNA from 18 to 19 GHz with a reflective waveguide termination.	30
3.11	Power flow in the rectangular waveguide [fW] at LNA from 18 to 19 GHz with a realistic waveguide termination.	31
3.12	Power flow in the rectangular waveguide [fW] at LNA from 18 to 19 GHz with a perfect waveguide termination.	31
A.1	S_{11} at output port with a fully reflective termination	36
A.2	S_{11} at output port with realistic termination	37

Chapter 1

Background

The He6-CRES experiment will perform high-precision β -decay spectroscopy of ${}^6\text{He}$ and ${}^{19}\text{Ne}$ through a frequency-based experimental technique called Cyclotron Radiation Emission Spectroscopy (CRES) [1]. The experiment is a low-energy probe of physics beyond the Standard Model, as distortions to the β spectrum may correspond to non-standard chirality-flipping scalar and tensor currents, parametrized by the Fierz interference term b_{Fierz} [2].

He6-CRES aims to perform a measurement of b_{Fierz} with sensitivity $\Delta b \lesssim 10^{-3}$, which would enable probes of new physics at the > 10 TeV scale [3].

1.1 Beta decay experiments and b_{Fierz}

Beta decay is a fundamental type of nuclear decay mediated by the weak interaction in which a nucleon releases a β^\pm particle (electron or positron) and a neutrino. β^- decay is described by the process $n \rightarrow p + e^- + \bar{\nu}_e$ via a W^- boson, and β^+ decay is $p \rightarrow n + e^+ + \nu_e$ via a W^+ boson. Due to the mass of the proton being greater than the mass of the neutron, free protons cannot undergo β^+ decay, so this process only affects protons in a nucleus.

Beta decays have been key to both theoretical and experimental breakthroughs in the development of modern particle physics and the theory of the standard Model. In 1930, Wolfgang Pauli hypothesized the existence of the neutrino (under the later-revised name of "neutron") to explain continuous beta energy spectra [4]. In 1956, the seminal Wu experiment [5] discovered that the weak interaction was parity violating by finding asymmetry in the angular dependence of ${}^{60}\text{Co}$ beta decay. Today, beta decay continues to provide insight into the Standard Model and is being used in experimental searches for physics Beyond the Standard Model (BSM).

In the Standard Model, weak interaction is described by vector-minus-axial vector (V-A) theory, which implies that weak interactions can only involve left-chiral fermions or right-chiral antifermions: parity is maximally violated and chirality is conserved. In some Beyond the Standard Model theories, new physics at energies beyond the electroweak symmetry breaking scale $\gtrsim 10$ TeV would violate chiral symmetry. In particular, some BSM extensions of the weak interaction include chirality-flipping scalar and tensor currents in addition to the existing V-A model. From Cirigliano et al. [6, 7, 3], a correspondence can be made between new physics at these high energies and distortions to low-energy (MeV-scale) nuclear

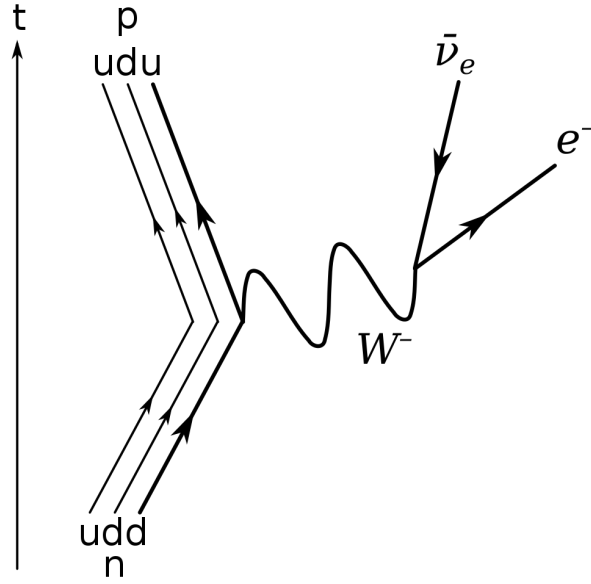


Figure 1.1: Feynman diagram of β^- decay

processes such as beta decay. The scalar and tensor coupling constants ϵ_S and ϵ_T contribute linearly to the Fierz interference term b_{Fierz} , a parameter which introduces an m/E distortion in the beta differential decay distribution. $b_{Fierz} = 0$ in the Standard Model.

$$\frac{dN_{obs}}{dE} = \frac{dN}{dE} \left(1 \pm b_{Fierz} \frac{m_e}{E} \right). \quad (1.1)$$

The sign of the b_{Fierz} distortion is + for β^- decays and - for β^+ decays. Furthermore, pure Fermi decays probe exclusive scalar currents ϵ_S , while pure Gamow-Teller decays probe exclusively tensor currents ϵ_T , and mixed transitions probe a linear combination of the two [7]. For example, ${}^6\text{He}$ decays via pure Gamow-Teller decay, ${}^{14}\text{O}$ decays via a pure Fermi decay, and free neutrons and ${}^{19}\text{Ne}$ have mixed decays.

It is established in [7, 3, 8] that experimental measurements of b_{Fierz} with uncertainties $\Delta b \lesssim 10^{-3}$ in beta decay experiments would achieve a sensitivity to physics at energy scales > 10 TeV. Current experimental limits on b_{Fierz} are set by ultracold neutron decay spectroscopy and angular correlation experiments such as UCNA and UCNb [2] at Los Alamos National Laboratory and Nab at Oak Ridge National Laboratory [9]. He6-CRES aims to reach 10^{-3} sensitivity from the beta decays of ${}^6\text{He}$ and ${}^{19}\text{Ne}$ using a frequency-based technique called Cyclotron Radiation Emission Spectroscopy.

1.2 Cyclotron Resonance Emission Spectroscopy

A particle with charge q and mass m (e.g. electron or positron, denoted β^\pm) in a magnetic field \vec{B} undergoes cyclotron resonance,

$$q\vec{v} \times \vec{B} = \gamma \frac{mv^2}{r}. \quad (1.2)$$

Taking $E = \gamma mc^2$, the frequency of cyclotron resonance f_c for a β^\pm with energy E is given by

$$f_c = \frac{|q| Bc^2}{2\pi E}. \quad (1.3)$$

The frequency of cyclotron resonance depends inversely on E . Measuring f_c is thus a proxy for measuring the energy of a β^\pm particle without directly interacting with it [10]. As a charged particle spins, it emits coherent circularly polarized electromagnetic radiation at the cyclotron frequency, which couple to the fundamental mode of a circular waveguide and are received by an antenna and amplified. The cyclotron frequency increases as the particle loses energy to radiation, so CRES events appear as chirped signals at the LNA output, with the start frequency as the figure of interest for beta spectroscopy. A short-time Fourier transform plots the frequency space representation of a CRES signal in time.

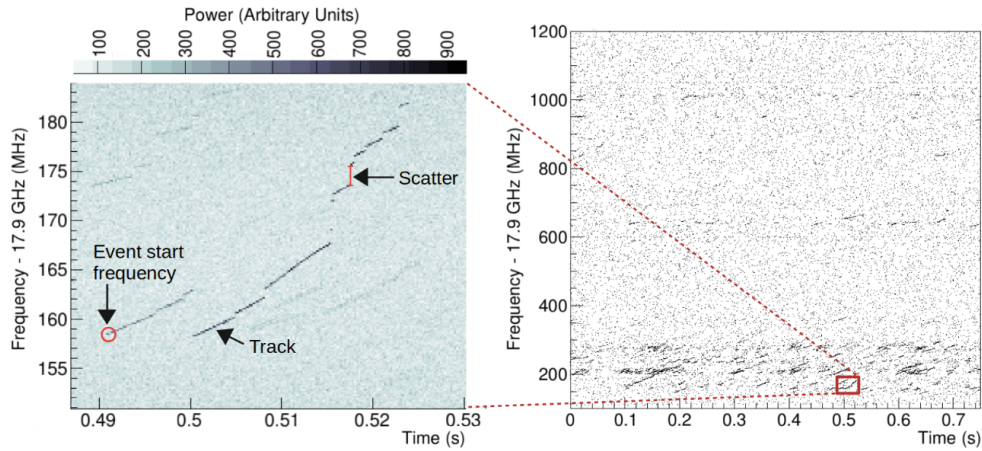


Figure 1.2: ^{83}Kr CRES data from [1]. Right: Spectrogram showing full 1.1 GHz bandwidth. Left: Zoom-in on a single CRES event

CRES was developed by the Project 8 experiment as a technique to directly measure the neutrino mass via the tritium β spectrum endpoint (18.6 keV). [11, 10], as a low-volume alternative to other precision β spectroscopy experiments such as KATRIN [12]. The He6-CRES experiment applies CRES over a much broader energy bandwidth, to measure full β spectra rather than just the endpoint.

CRES has various advantages compared to traditional β calorimetry methods. Experiments that involve depositing energy in a semiconductor or scintillator detector must account for losses such as backscattering and bremsstrahlung, and energy resolution is limited by the detector material. CRES does not directly measure β interactions with matter, and energy resolution is fixed by the frequency resolution of the Fourier transform applied to the amplifier readout [1].

1.3 Theory of waveguides

A plane wave propagating losslessly along the z -axis has a harmonic time and z dependence as $e^{i(\omega t - \beta z)}$, where the propagation constant $\beta = \frac{2\pi}{\lambda} = \frac{\omega}{v_p}$, carrying a wave number $k = \frac{2\pi}{\lambda_0} = \frac{\omega}{c}$,

where λ is the physical (peak-to-peak) wavelength, v_p is the phase velocity, λ_0 is the free-space wavelength of a plane wave with frequency ω , and $c = \frac{1}{\sqrt{\epsilon\mu}}$ [13]. Representing the wave as a phasor and omitting the time-dependent term, the phase of the wave is $\phi(z) = \beta z$, and the phase shift picked up over a distance of L is accordingly $\phi = \beta L$.

In a TEM structure (e.g. coplanar waveguide or free space), $\beta = k$. For TE or TM waves, as in circular and rectangular waveguides, this simplifying relationship does not hold, instead propagation is described by the cutoff wavelength k_c , such that [13]

$$k_c^2 = k^2 - \beta^2. \quad (1.4)$$

To support $e^{i\beta z}$ propagation through a waveguide, it is required that β be real, equivalently

$$\beta^2 = k^2 - k_c^2 > 0. \quad (1.5)$$

k_c is determined by solving Maxwell's Equations inside the specific geometry of the waveguide, and depends on the waveguide dimension mode indices (n, m) . With R as the inner radius of the circular waveguide, a and b as the inner dimensions of the rectangular waveguide along x and y respectively, [13]

$$k_c = \sqrt{\left(\frac{n\pi}{a}\right)^2 + \left(\frac{m\pi}{b}\right)^2} \quad (\text{rectangular waveguide}), \quad (1.6)$$

$$k_c = \frac{p_{nm}}{R} \quad (\text{circular waveguide, TM}_{nm}), \quad (1.7)$$

$$k_c = \frac{p'_{nm}}{R} \quad (\text{circular waveguide, TE}_{nm}). \quad (1.8)$$

Here, p_{nm} and p'_{nm} denote the m th zero of the Bessel function of the first kind $J_n(x)$ and its derivative $J'_n(x)$.

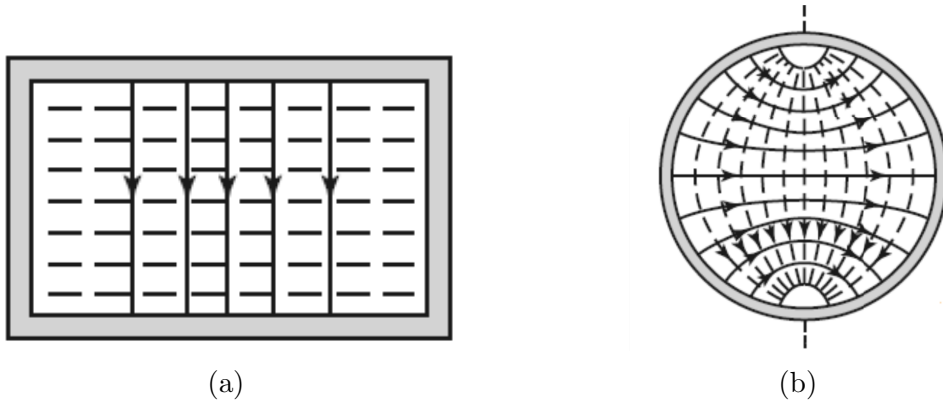


Figure 1.3: Cross section of TE_{10} in a rectangular waveguide (a) and TE_{11} in a circular waveguide, polarized along x (b) [14]

The fundamental mode of a waveguide is the mode with the lowest cutoff wave number. In a rectangular waveguide, the fundamental mode is (taking $a > b$ without loss of generality) the TE_{10} mode, with $k_c = \frac{\pi}{a}$ (Fig. 1.3a). In a circular waveguide, this is the TE_{11} mode, with $k_c \approx \frac{1.8412}{R}$, depicted in Figure 1.3b. This mode is degenerate with continuous polar symmetry, so it is conventionally analyzed as two orthogonal polarizations along x and y .

1.3.1 Power flow and attenuation in waveguides

We may define the Poynting vector as

$$\vec{S} = \vec{E} \times \vec{H}^*. \quad (1.9)$$

From this expression, the power flow along the the waveguide through a cross section A_0 perpendicular to the direction of propagation \hat{z} is given by

$$P = \frac{1}{2} \operatorname{Re} \int_{A_0} \vec{E} \times \vec{H}^* \cdot \hat{z} dA. \quad (1.10)$$

The factor of $\frac{1}{2}$ corresponds to the root-mean-squared time averaging of the electric and magnetic fields.

The propagation constant $i\beta$ is often generalized to include an attenuative term $\gamma = \alpha + i\beta$, arising from propagation through a lossy medium. Attenuation in waveguides occurs from dielectric loading or from Ohmic conductor losses. Since the He6-CRES waveguides are evacuated, attenuative losses are attributed to conductor losses only. The Ohmic attenuation term for TE $_{n,m}$ and TM $_{n,m}$ modes in a circular waveguide can be approximated for $\omega > k_{c_{n,m}} c$ [15], where $\eta = \sqrt{\mu_0/\epsilon_0}$ is the impedance of free space and $R_s = \sqrt{\omega\mu_0/2\sigma}$ is the surface resistance of the waveguide walls, with finite electrical conductivity σ :

$$\alpha_c = \frac{R_s \omega}{a \eta \beta_{n,m} c} \begin{cases} \left(\frac{k_{n,m} c}{\omega} \right)^2 + \frac{n^2}{p_{n,m}^2 - n^2} & \text{TE} \\ 1 & \text{TM.} \end{cases} \quad (1.11)$$

More strictly, conductive waveguide walls modify the boundary conditions at the waveguide walls, perturbing the TE and TM mode basis and thus the power flow along the waveguide, which were both previously taken to be ideal in deriving Eqn. 1.11. The approximation fails when ω is very close to ω_c , and when $\omega < \omega_c$ the finite conductivity allows for a small amount of power to flow down the waveguide as current induced in the skin depth of the conductor walls. Methods to construct to the modified mode basis and derive more accurate expressions for α_c are described in e.g. [16]. A more detailed discussion of power flow in CRES experiments including these attenuation effects is in preparation [17].

1.4 He6-CRES waveguide system

A diagram of the Phase II He6-CRES RF system is given in Figure 1.4. CRES events occur in the decay cell (**A**), which contains the gaseous β emitter. CRES radiation leaves the decay cell and passes through a circular-to-linear polarizer (**B**). The linearly polarized wave passes through a waveguide transition (**C**) to a rectangular waveguide (**D**), to a microwave circulator coupling the rectangular waveguide to RF low-noise amplifiers (LNAs) (**E**). CRES radiation leaving the decay cell in the opposite direction propagates through a circular waveguide to a waveguide terminator (**F**).

In the previous iteration of the experiment (Phase I), the two sides of the decay cell had symmetric RF systems apart from the waveguide U-bend. An additional circular-to-linear polarizer and circular-to-rectangular waveguide adapter were installed on the left side of the

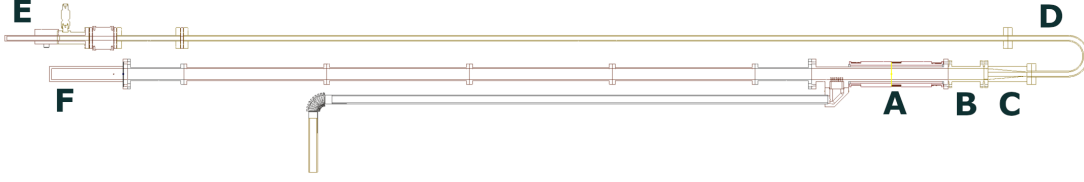


Figure 1.4: Diagram of He6-CRES system. **A**: Decay cell. **B**: Polarizer. **C**: circular-to-rectangular waveguide transition. **D**: Rectangular waveguide. **E**: to LNAs. **F**: circular waveguide terminator.

decay cell **A**. Instead of a terminator at **F**, a second RF amplifier system read CRES data in parallel to the readout at **E**.

The amplifier readout is digitized at 2400 MHz in bins of 2^{13} samples. The Fourier transform of the binned data forms a 2D plot of Fourier amplitude in frequency and time.

1.5 RF network parameters

1.5.1 Scattering parameters

Scattering parameters (S-parameters) are a type of linear network parameter that relate the amplitudes of incident (a_i) and reflected (b_i) waves at each port of a microwave network. S-parameters describe how much a wave incident on any one port excites a wave leaving a specific port. By using field amplitudes, S-parameters bypass the ambiguity of defining voltage and current in non-TEM structures, and lend themselves especially well to analysis of components at microwave frequencies. A typical 2-port microwave network is depicted in Figure 1.5.

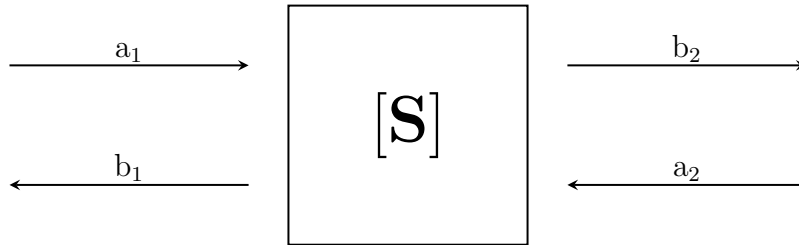


Figure 1.5: 2-port S-parameters, with incident and reflected field amplitudes a_n and b_n

The S-parameters for a 2-port network are defined as:

$$\begin{pmatrix} b_1 \\ b_2 \end{pmatrix} = \begin{bmatrix} S_{11} & S_{12} \\ S_{21} & S_{22} \end{bmatrix} \begin{pmatrix} a_1 \\ a_2 \end{pmatrix} \quad (1.12)$$

In the canonical 2-port example, $S_{11} = \left. \frac{b_1}{a_1} \right|_{a_2=0}$ is the reflection at port 1 when port 2 is terminated, and $S_{21} = \left. \frac{b_2}{a_1} \right|_{a_2=0}$ is the transmission from port 1 to port 2 when port 2 is terminated.

A general N -port network can be described by the following S-parameter matrix. Generally, S_{ij} expresses how much a signal incident on port j excites a wave at port i , when all ports other than j have zero incident signal.

$$\begin{pmatrix} b_1 \\ \vdots \\ b_n \end{pmatrix} = \begin{pmatrix} S_{11} & \cdots & S_{1n} \\ \vdots & \ddots & \vdots \\ S_{n1} & \cdots & S_{nn} \end{pmatrix} \begin{pmatrix} a_1 \\ \vdots \\ a_n \end{pmatrix} \quad (1.13)$$

Using 4-port networks is natural for analyzing series RF elements in the He6-CRES experiment. The fundamental mode of a circular waveguide is the TE_{11} mode, which is degenerate with polar symmetry. We decompose this mode into orthogonal x and y polarizations, which can be treated as two independent “virtual” ports at the same “physical” port. In this sense, a two-ended component in a circular waveguide can be analyzed as a balanced 4-port network.

Borrowing terminology from the theory of coupled antennas, we introduce the notion of Active S parameters to describe transmission and reflection of a circularly polarized wave through a component. Active S parameters describe a weighted sum of a devices S-parameters under a certain excitation times the magnitude and phase of that excitation. A circularly polarized wave is a superposition of an x-polarized and y-polarized wave with equal magnitude and 90° phase difference, so we can write

$$\text{Active } S_{ij} = \frac{E_x S_{ij,x} + E_y S_{ij,y}}{|E_x|^2 + |E_y|^2} = \frac{S_{ij,x} \pm i S_{ij,y}}{\sqrt{2}}, \quad (1.14)$$

Where $S_{ij,x}$ and $S_{ij,y}$ are the S parameters under an x-polarized and y-polarized incident wave respectively. The $\pm i$ phase is for right handed ($+i$) and left handed ($-i$) circular polarization.

1.5.2 Transfer scattering parameters

Transfer scattering parameters, or T-parameters, are another wave-amplitude network parameter that facilitate characterizing the overall performance of several “cascaded” microwave networks in series [14]. T-parameters allow for cascading microwave networks in close analogy to using ABCD network parameters for cascading 2-port lumped element networks. For a two-port network, the T-parameters are defined as ¹

$$\begin{pmatrix} b_1 \\ a_1 \end{pmatrix} = \begin{bmatrix} T_{11} & T_{12} \\ T_{21} & T_{22} \end{bmatrix} \begin{pmatrix} a_2 \\ b_2 \end{pmatrix} \quad (1.15)$$

Consider two two-port networks with T-parameters T_1 and T_2 . The T-parameter matrix describing the series combination of the two networks is simply $T = T_1 T_2$, and this cascading extends to an arbitrary number of networks in series. Most importantly, while T-parameters cannot be physically measured in the same way as S-parameters, there exists a well-known

¹Some conventions reverse the order of b_1 and a_1 on the left-hand side and a_2 and b_2 on the right, yielding different but equivalent notation in (1.16).

conversion between S-parameters and T-parameters [14],

$$\begin{aligned}
 T_{11} &= S_{12} - \frac{S_{11}}{S_{22}} S_{21} & S_{11} &= \frac{T_{12}}{T_{22}} \\
 T_{12} &= \frac{S_{11}}{S_{21}} & S_{12} &= T_{11} - \frac{T_{12} T_{21}}{T_{22}} \\
 T_{21} &= -\frac{S_{22}}{S_{21}} & S_{21} &= \frac{1}{T_{22}} \\
 T_{22} &= \frac{1}{S_{21}} & S_{22} &= -\frac{T_{21}}{T_{22}}
 \end{aligned} \tag{1.16}$$

Using these conversions, we can obtain “overall” S-parameters of a series of cascaded microwave networks with known S-parameters $[S_1], \dots, [S_N]$ by following a simple algorithm:

1. Using S to T transformations from (1.16), convert each $[S_1], \dots, [S_N]$ to T-parameters $[T_1], \dots, [T_N]$.
2. Calculate the overall T parameters of the entire network with simple matrix multiplication

$$[T] = \prod_n [T_n].$$

3. Using T to S transformations from (1.16), convert T to the overall network S parameters.

This overall S-parameter matrix takes into account the full wave behavior throughout the whole network naturally from the T-parameter chaining, without additional analysis needed.

1.5.3 Generalizing to N -port networks

Recent studies [18, 19] explore the idea of generalizing the traditional two-port T-parameter definition to a cascaded series networks with $N > 2$. The S-parameter matrix of an N -port network remains square ($N \times N$) for all N . The definition of the T-parameters implicitly requires denoting ports as input (“external”) ports or output (“internal”) ports for cascading, so in unbalanced networks with a different number of internal and external ports the input/output symmetry is broken [18]. An unbalanced network will thus have a non-square T-matrix. However, balanced networks still have a square T-parameter matrix, and we will limit the scope of this discussion to balanced 4-port networks, with two external ports and two internal ports. The T-parameter matrix for such a network with external ports 1,2 and internal ports 3,4 is

$$\begin{pmatrix} b_1 \\ b_2 \\ a_1 \\ a_2 \end{pmatrix} = \begin{bmatrix} T_{11} & T_{12} & T_{13} & T_{14} \\ T_{21} & T_{22} & T_{23} & T_{24} \\ T_{31} & T_{32} & T_{33} & T_{34} \\ T_{41} & T_{42} & T_{43} & T_{44} \end{bmatrix} \begin{pmatrix} a_3 \\ a_4 \\ b_3 \\ b_4 \end{pmatrix} \tag{1.17}$$

Cascading 3 such networks is schematically represented in Figure 1.6.

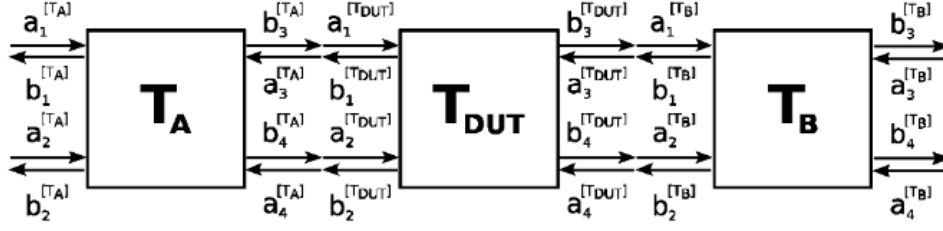


Figure 1.6: Cascading three 4-port balanced networks with T-parameters [18]

Working with ports assigned as external or internal, N -port network parameters may be either between two external ports (external-to-external), between two internal ports (internal-to-internal), internal-to-external, or external-to-internal. Notice that a multiport network parameter matrix can be decomposed into submatrices of parameters that fall in the same “group” of input and output ports, as in (1.18).

$$S = \begin{bmatrix} [S_{ee}] & [S_{ei}] \\ [S_{ie}] & [S_{ii}] \end{bmatrix} \quad T = \begin{bmatrix} [T_{ee}] & [T_{ei}] \\ [T_{ie}] & [T_{ii}] \end{bmatrix} \quad (1.18)$$

It can be shown [18, 19] that not only does a transformation between N -port S- and T-parameters exist, it generally preserves much of the familiar structure of (1.16).

$$\begin{aligned} T_{11} &= S_{ei} - S_{ee}S_{ie}^{-1}S_{ii} & S_{ee} &= T_{ei}T_{ii}^{-1} \\ T_{12} &= S_{ee}S_{ie}^{-1} & S_{12} &= T_{ee} - T_{ei}T_{ii}^{-1}T_{ie} \\ T_{21} &= -S_{ie}^{-1}S_{ii} & S_{21} &= T_{ii}^{-1} \\ T_{22} &= S_{ie}^{-1} & S_{22} &= -T_{ii}^{-1}T_{ie} \end{aligned} \quad (1.19)$$

1.5.4 Observed SNR oscillations

In the initial He6-CRES data collection stage (Phase I), we observed a strong frequency-dependent oscillations in the signal-to-noise ratio (SNR), as shown in Figure 1.7 at various B-field strengths. These oscillations are characteristic of internal reflections of CRES radiation off of various components in the RF assembly causing constructive and destructive interference of the signal. SNR variations interfere with accurate CRES event reconstruction, limiting our sensitivity to b_{Fierz} . It is therefore critical for the experiment to exhibit uniform and sufficiently high SNR over the frequency range of interest. The waveguide terminator at point F of Figure 1.4 was installed to mitigate these reflections, but the SNR oscillations remained a prominent feature of the experimental data (Fig. 1.8). The dominant oscillation peaks are spaced by about 90 MHz, corresponding to an interference with a path length on the order of twice the distance between the decay cell and the waveguide termination. This work contributes to efforts to understand and characterize the SNR oscillations and to suggest future hardware upgrades.

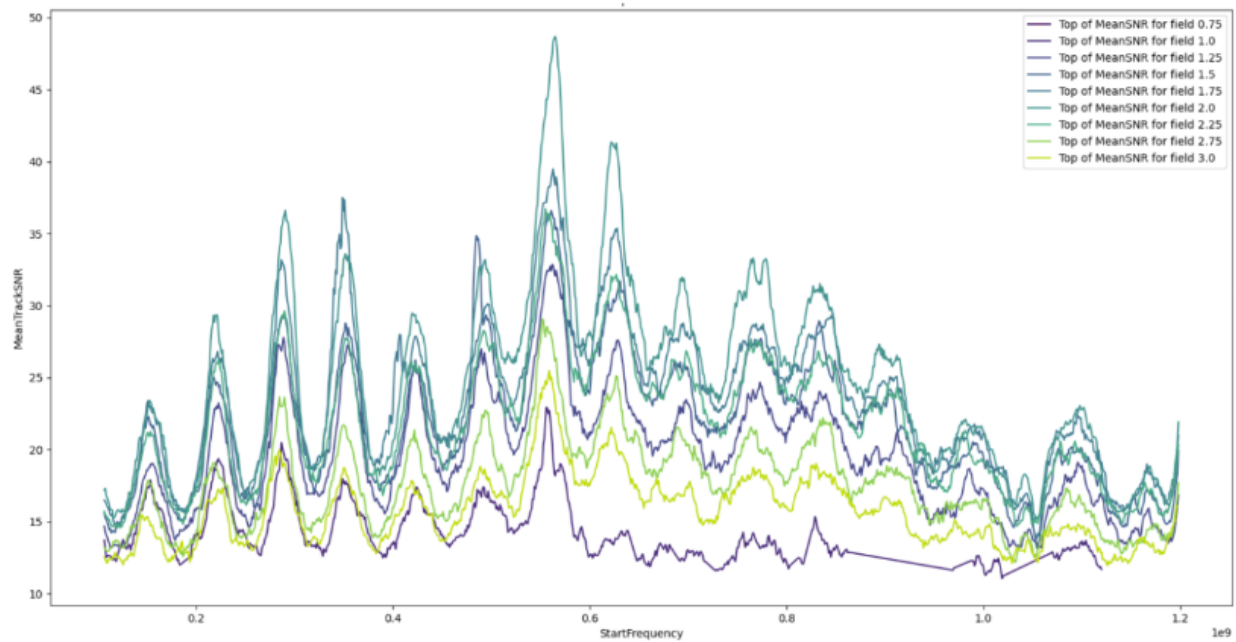


Figure 1.7: SNR vs. frequency varying magnetic field strength, before installing terminator

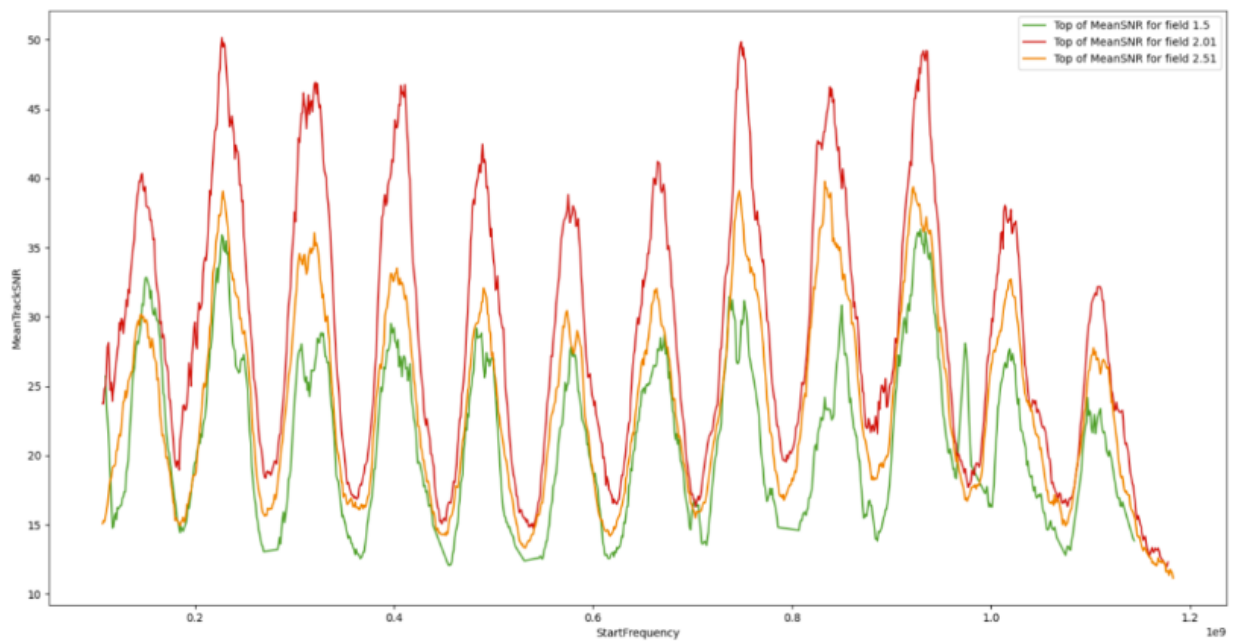


Figure 1.8: SNR vs. frequency varying magnetic field strength, with terminator

Chapter 2

Methods

Full-wave simulations of the RF components were performed in Ansys HFSS, a finite-element method solver for full-wave electromagnetic simulations [20], particularly well-suited to modeling high-frequency RF and microwave applications. All relevant components were modeled in the native 3D CAD environment, and assigned conductive or dielectric material properties or boundary conditions as needed. Copper waveguide material was frequently approximated as a perfect electrical conductor (PEC) material in the interest of computation time, except when investigating attenuation effects from conductor losses.

2.1 Simulating individual components

Waveguide components were first simulated individually to characterize their reflective and transmissive properties as S-parameters. Models of the circular-to-linear polarizer, waveguide transition, and circular waveguide termination were performed. The S-parameters of polarizer and waveguide transition in series were simulated directly in HFSS and calculated using transfer scattering parameters. Additional analysis was performed to characterize the behavior of this component assembly under a circularly polarized incident wave, intended as a proxy for CRES radiation.

The waveguide structure enclosing each component was assigned wave-port excitations at either end, which instructs HFSS to numerically solve for the modes of the waveguide in order of increasing cutoff frequency, then to express the S-parameters of the structure in terms of the waveguide modes at the port. Ansys HFSS reports S-parameters for each mode of each physical port of the structure being simulated. For legibility, this report attempts to retain the familiar two-port language (S_{11} , S_{12} , S_{21} , and S_{22}) with an additional qualifier for the polarization of the mode in question, rather than use 4-port notation.

The He6-CRES waveguide system is constructed with WR42 rectangular waveguides (internal dimensions $0.42'' \times 0.17''$) and $0.455''$ diameter circular waveguides.

2.1.1 Circular-to-linear polarizer

The polarizer applies a 90° relative phase shift between orthogonal components of a wave at 45° relative to the orientation of the polarizer. This allows for the conversion of circularly

polarized waves to linearly polarized waves as well as the reverse. Especially in free space, quarter-wave polarization is performed with a birefringent crystal [21], but the He6-CRES polarizer is a diamond-shaped dielectric sheet inside a circular waveguide (diameter 0.455"), for improved broadband performance (Fig. 2.1), for a vacuum to be pulled in the waveguide, and to remove reflections that would otherwise occur at the vacuum-crystal interface.

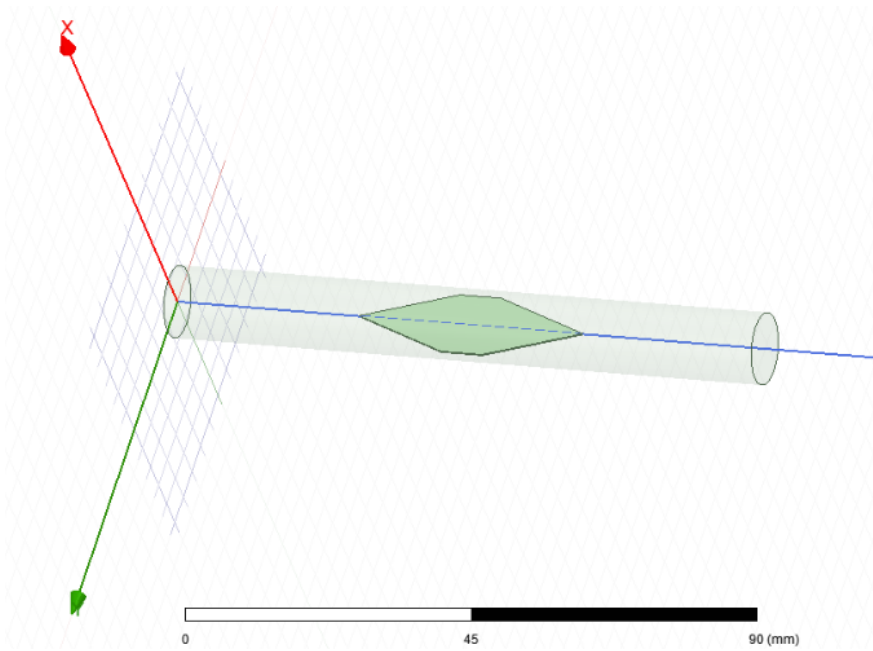


Figure 2.1: Polarizer model in HFSS, with waveguide walls hidden

Under a linearly polarized incident wave, the circularly polarized output of a perfect polarizer could be decomposed into x- and y- linearly polarized components, each carrying half the incident power. $|S_{21}|$ into each polarization is therefore $0.5 \approx -3.01$ dB. We may also measure the quality of elliptical polarization with the phase difference between S_{21} into both x- and y-polarized modes from either an x- or y- linearly polarized incident wave. The phase difference between these two parameters is 90° in a perfect polarizer.

The axial ratio is another figure of merit for polarization quality, defined as the ratio between the major and minor axis amplitudes of an elliptically polarized wave. Perfect circular polarization has an axial ratio of 0 dB, and by convention a practical circularly polarized wave is understood to have an axial ratio < 3 dB. The axial ratio r can be related to a measurement known as cross-polar distortion (XPD) with the following equation:

$$\text{AR [dB]} = 20 \log_{10} \left(\frac{1 + \text{XPD}}{1 - \text{XPD}} \right) \quad (2.1)$$

XPD is defined as the ratio of the amplitudes of right-hand circularly polarized and left-hand circularly polarized components of a wave, squared.

$$\text{XPD} = \frac{|E_{\text{RHCP}}|^2}{|E_{\text{LHCP}}|^2} \quad (2.2)$$

The circularly polarized components can be constructed from the S-parameters from a linearly polarized incident wave into the x- and y-polarized components of the output wave. These are simply the Active S_{21} parameters of the polarizer for RHCP and LHCP incident waves.

$$E_{\text{RHCP}} = \frac{S_{21,x} + iS_{21,y}}{\sqrt{2}} \quad (2.3)$$

$$E_{\text{LHCP}} = \frac{S_{21,x} - iS_{21,y}}{\sqrt{2}} \quad (2.4)$$

2.1.2 Circular-to-rectangular waveguide transition

The circular-to-rectangular transition is a continuous deformation from a circular waveguide to a WR-42 rectangular waveguide. Notably, only the fundamental TE_{10} mode of a rectangular WR-42 waveguide has a cutoff frequency below our frequency range of interest, at 14.05 GHz. The next mode, TE_{20} , has a cutoff frequency of 28.10 GHz. The TE_{01} mode has a cutoff frequency of 34.71 GHz, and is of more interest than the TE_{20} mode as it is orthogonal to the TE_{10} . Components of a wave that project onto non-propagating modes reflect, so this component is of interest as the first obvious location where high reflection may occur the apparatus.

The model (Fig. 2.2) is oriented so the E-field of the propagating TE_{10} is parallel to the y-axis. We anticipate an incident wave linearly polarized along y to transmit. The non-propagating TE_{01} mode has an E-field parallel to x, so x-polarized waves are expected to reflect.

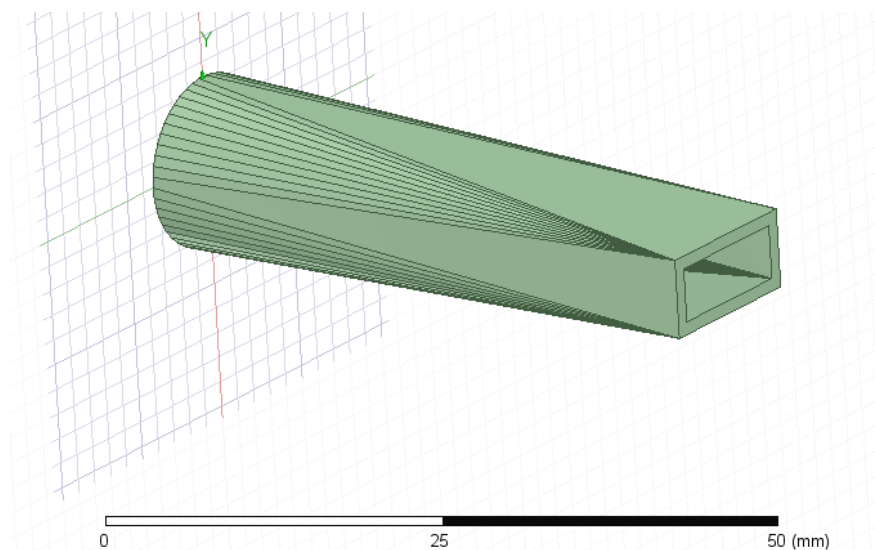


Figure 2.2: Circular-to-rectangular waveguide transition model in HFSS

A recent update to the HFSS geometry kernel changed the behavior of the loft feature to generate a continuous 3D shape between two planar cross sections. Lofting between a curve and a polygon is no longer supported, so the waveguide transition was constructed with an $N = 50$ regular polygon cross section on the circular waveguide side.

2.1.3 Waveguide termination

In Phase II, the waveguide extending from the decay cell away from the U-bend waveguide (I-side) is a circular waveguide ending at a conical waveguide termination made of a blend of graphite powder and Stycast 1266 epoxy, with an estimated dielectric constant. The termination is intended to absorb CRES radiation from the decay cell without reflection. The design is based on the Project 8 waveguide termination, which estimates an effective dielectric constant of $\epsilon_{eff} \approx 3.1 + 0.033i$ with the Maxwell Garnett formula for the dielectric constant of mixed media [22]. The spacing of the SNR oscillation peaks indicates the presence of a long reflecting cavity being formed, most probably explained by imperfect termination and partial reflection at this component.

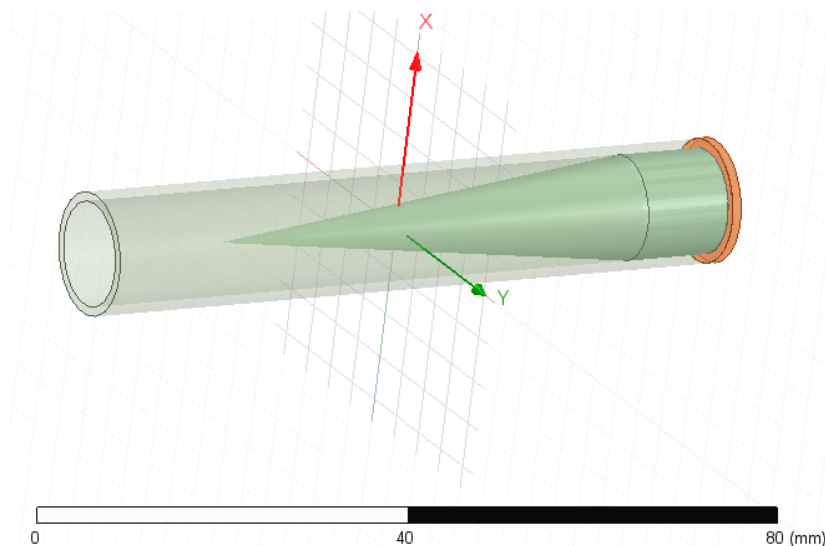


Figure 2.3: Conical waveguide termination model with backing PEC cap in orange in HFSS

2.2 Modeling the full waveguide system

After characterizing individual components in HFSS, the next step was to produce a full model of the He6-CRES waveguide system, including the decay cell and CRES source. With a complete model, we may study the impact of modifications to the components or system configuration before making expensive and time-consuming hardware upgrades.

2.2.1 Defining a CRES source

Using wave port sources is insufficient for simulating the full RF model, which includes the decay cell. In HFSS, wave ports are intended to be placed on the external surface of a model and represent an external source. Internal wave ports are supported, but require a PEC backing plane of the same cross section, which would cause full reflection of any radiation crossing the decay cell. At frequencies above the TM_{11} cutoff, cyclotron radiation also does

not excite a pure mode in the circular waveguide like a wave port would, and instead is a superposition of modes including those above TE_{11} at harmonics of the cyclotron frequency.

HFSS does not support point particle sources or moving charges, but it does support assigning explicit near-field electric and magnetic field vectors to a surface as a Linked Field excitation. To model a CRES source, we imported the electric and magnetic fields of a radiating point charge inside a waveguide, numerically evaluated at discrete solution frequencies between 18 and 19 GHz in 20 MHz intervals. The fields were calculated on a lattice of points specified on the surface of a source geometry, and stored in the `.nfd` data format and imported to Ansys with a `.and` header file. Magnetic bottle trap effects were not considered, and the β was assumed to be centered on the waveguide and have a 90° pitch angle. The simulation was performed at each solution frequency for which we generated the source fields.

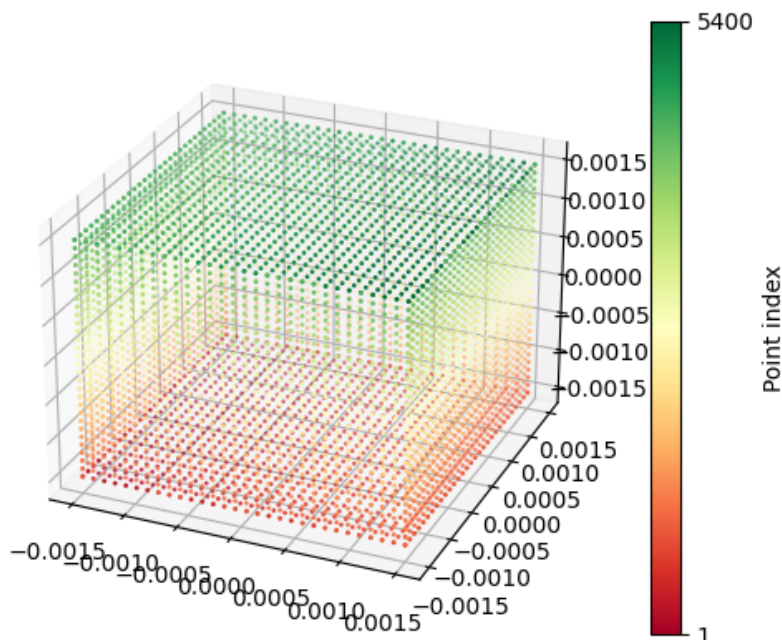


Figure 2.4: Lattice of points on the surface of a 3mm cube on which the near-field source is defined. Points are spaced by 0.1 mm and colored by index.

For each frequency specified in the near field solution, the `.nfd` file format specifies a solution frequency then iterates through each point on the lattice. Each line contains 16 comma-separated values: the index of a lattice point in the order they are defined, the point position, and the real and imaginary components of the \vec{E} and \vec{H} vector components. Cartesian, spherical, and cylindrical coordinate systems are supported, and the lattice may be specified on a cube, sphere, cylinder, or plane.

The `.and` file format links a `.nfd` file to an HFSS solution setup. It contains a header block, which details the solution frequencies and source geometry, and as a data block, which points to a `.nfd` file for each solution frequency.

Although a cylindrical source geometry would be natural for the system, we were not able to successfully import CRES near-field solutions specified on spherical or cylindrical source geometry. The success of the near-field linking seems to depend on the order points are defined and indexed in the solution lattice, and we were not able to specify a mesh on a curved surface that did not result in an error. Because of this, simulations were performed with fields defined on a 3mm side length cube source at the center of the decay cell.

After generating the near fields in a `.nfd` file and the associated `.and` file, the source was imported into HFSS. A 3mm cube was modeled and assigned a near field excitation with the context menu `Excitations > Linked Field > Near Field ... > Interior Source` and selecting the `.and` file. With this command, HFSS creates a PEC copy of the source geometry and assigns the source excitation to it. The original model of the cube was set to a non-Model geometry to not interfere with the source.

2.2.2 HFSS waveguide model

The full waveguide system as shown in Figure 1.4 was modeled in Ansys HFSS. The electromagnetic model omits the pipe that delivers the isotopes to the decay cell, the flanges connecting waveguide components, and the RF circulator coupling the rectangular waveguide to the LNA output.

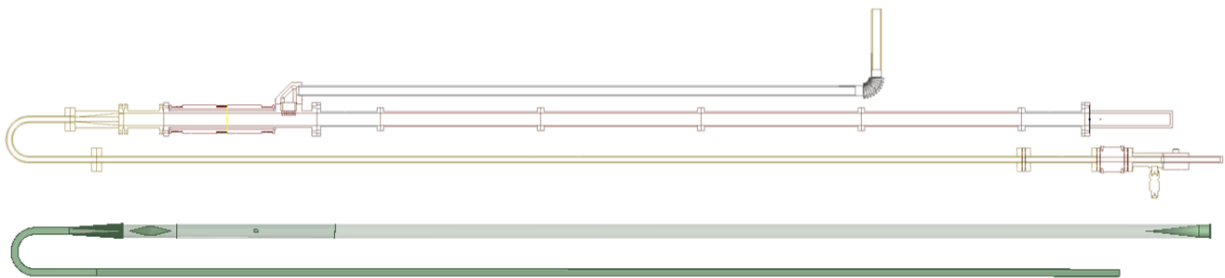


Figure 2.5: Cross section of actual He6-CRES waveguide system (top) compared to HFSS model

The system was simulated with three different circular waveguide terminations. First, we used the realistic termination model described in 2.1.3, then we used a "worst case" perfectly reflective waveguide termination by removing the graphite-epoxy terminator cone and leaving only flat PEC wall at the end of the waveguide. Finally, we replaced the PEC wall with a waveport, which behaves like an infinite waveguide or a perfect termination for a "best case" result.

2.2.3 Power delivered to amplifier

The signal strength recorded at the RF LNAs is related to the power delivered to the read-out antennas. This is measured in simulation by integrating the time-averaged Poynting flux through waveguide cross section at the end of the waveguide, by Eqn. 1.10. The numerical surface integral is computationally expensive on the generated FEM mesh, and must be repeated at each solution frequency specified in simulation. To make the computation

tractable, we exploit the y -independence of S_z for the propagating TE_{10} mode in a rectangular waveguide (Figure 2.6).

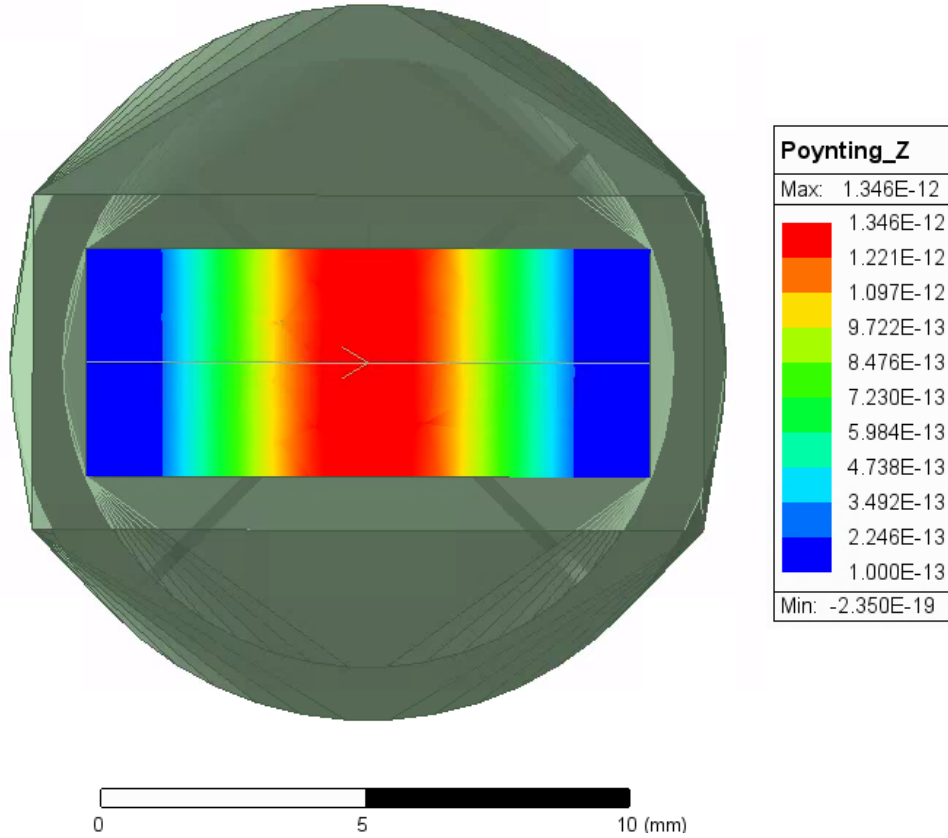


Figure 2.6: Real component of S_z [W/m^2] over the WR42 waveguide cross section, with $y = 0$ integration line traced.

$$P = \frac{1}{2} \operatorname{Re} \int_{-\frac{b}{2}}^{\frac{b}{2}} \int_{-\frac{a}{2}}^{\frac{a}{2}} S_z(x) dx dy = \frac{b}{2} \operatorname{Re} \int_{-\frac{a}{2}}^{\frac{a}{2}} S_z(x) dx \quad (2.5)$$

The numerical integral in one spatial dimension is much quicker than the the surface integral. This calculation is performed with the HFSS Fields Calculator utility, which allows defining a wide range of expressions based on environment variables and simulated electromagnetic fields. The expression for Poynting flux in the Fields Calculator notation, which uses Reverse Polish Notation operations, is

`*(Integrate(Line(integration_line),Real(ScalarZ(Poynting))),$y_wr42)$`,
 where `integration_line` is a line object over which the integration is performed (see Fig. 2.6) and `$y_wr42` is a constant environment variable defined as the height b of the WR42 waveguide. The `Poynting` field solution variable is a time-averaged value that already contains the scaling factor of $\frac{1}{2}$ and is automatically computed by HFSS at simulation time.

Chapter 3

Results

3.1 Simulating individual components

3.1.1 Circular-to-linear polarizer

The polarizer S_{11} and S_{21} for both x-polarized and y-polarized incident waves are presented below. Input reflection is below -25 dB for all polarizations and transmission from each incident polarization is approximately -3 dB (half power): the incident linearly polarized wave becomes a superposition of x and y polarized waves.

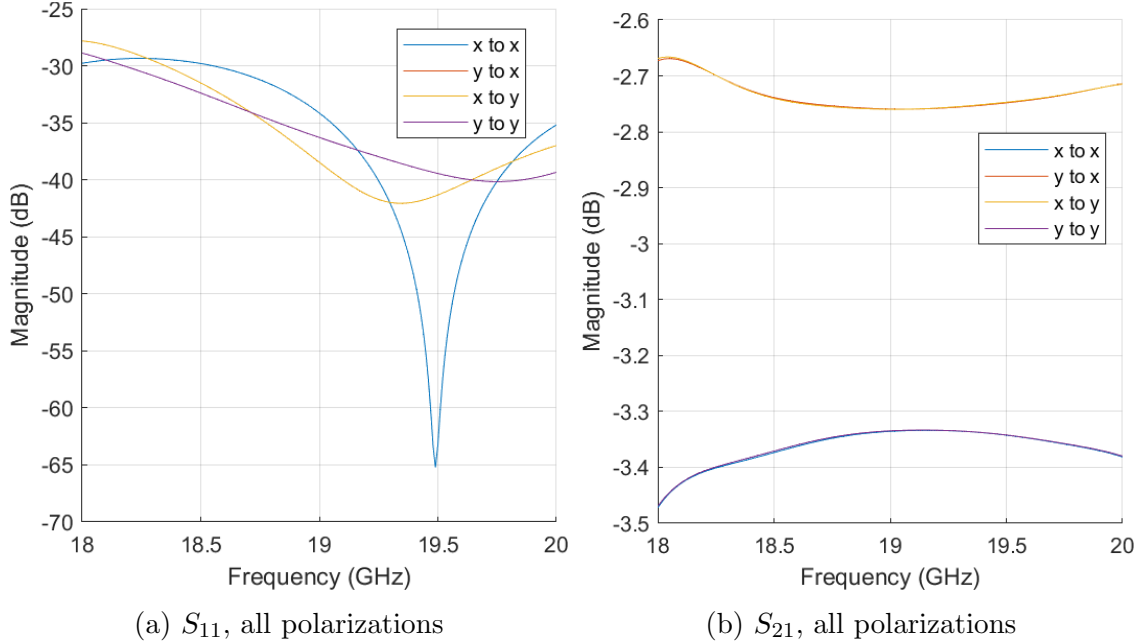


Figure 3.1: Polarizer S_{11} and S_{21}

When a linearly polarized wave is converted into a circularly polarized wave, a relative phase shift of 90° is applied. This result is confirmed by calculating the phase difference between S_{21} into the x-polarized mode and y-polarized mode.

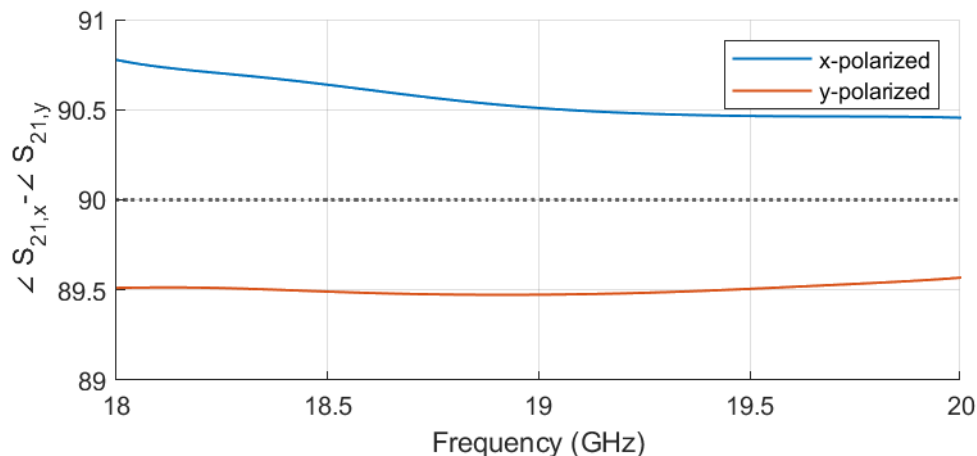


Figure 3.2: Polarizer phase shift along x and y

We also calculate the axial ratio of the output wave from the S_{21} to measure the quality of polarization.

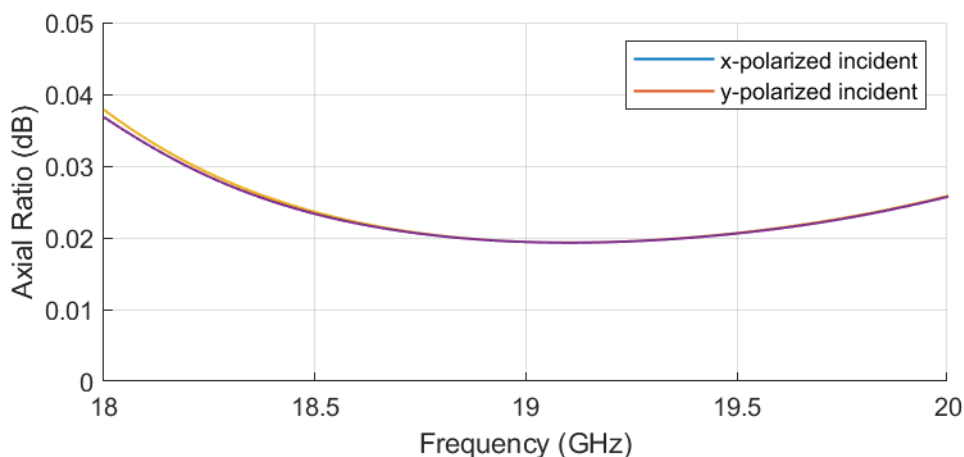


Figure 3.3: Polarizer axial ratio

These results all suggest that the polarizer is performing according to specification: it has very low input reflection and performs nearly perfect polarization.

Using Active S parameters, we can determine how the polarizer affects an incident circularly polarized wave. In Figure 3.4, we see that a RHCP wave transmits very well (j -0.05 dB) into the x-polarized TE_{11} mode and very little (j -26 dB) into the y-polarized mode, and a LHCP wave likewise transmits very purely into the y-polarized mode and transmits very little into the x-polarized mode.

3.1.2 Circular-to-rectangular waveguide transition

The S_{11} and S_{21} of the waveguide transition are presented below with the circular waveguide side as the input port and the rectangular waveguide TE_{10} mode as the output port. An incident x-polarized wave in the circular waveguide does not excite the TE_{10} mode and

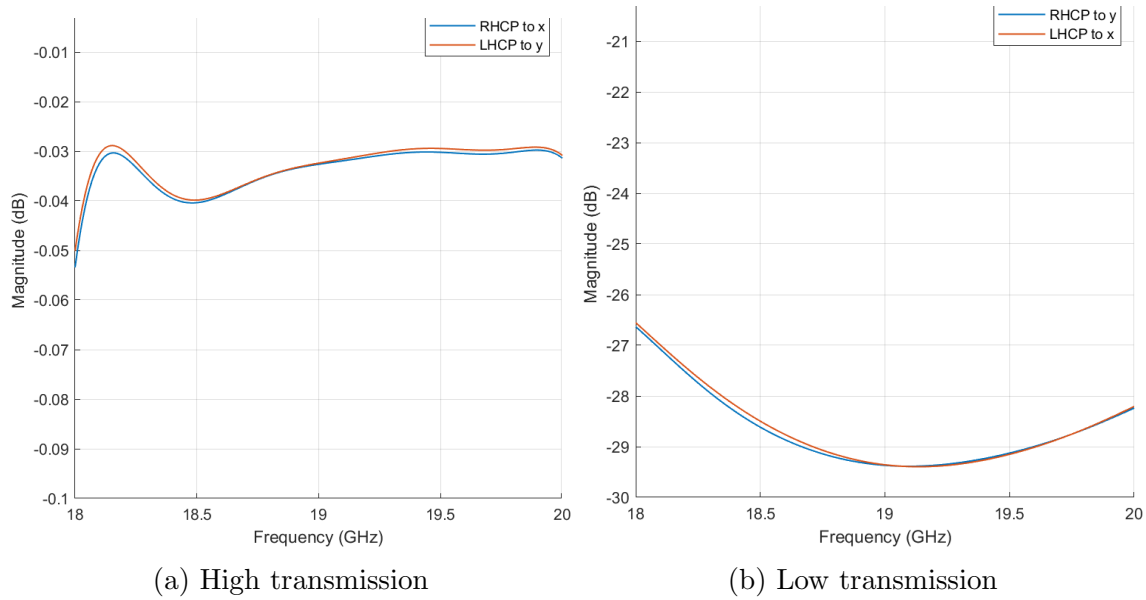


Figure 3.4: Active S_{21} of RHCP and LHCP waves transmitting to x- and y-polarized mode in the polarizer

reflects completely, as seen by the high x-to-x S_{11} and low S_{21} . By contrast, the y-polarized mode transmits completely into the TE_{10} mode.

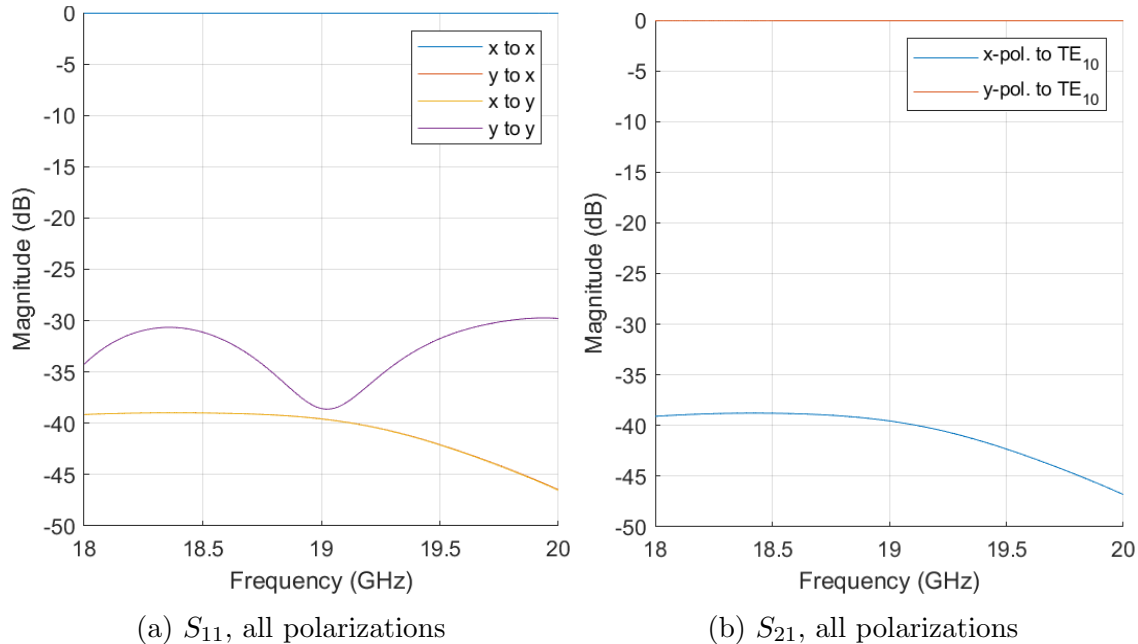


Figure 3.5: Waveguide transition S_{11} and S_{21}

3.1.3 Behavior in series

The overall S parameters of the polarizer and waveguide transition in series were constructed using the T parameters of each component. From this, we calculate the Active S parameters of the series components. We found that the waveguide transition only transmits y-polarized incident waves, while x-polarized waves cannot propagate in the rectangular guide. We also found that the polarizer converts LHCP waves to the y-polarized TE_{11} mode and RHCP waves to the x-polarized TE_{11} mode. Therefore, we are expecting to see high transmission of an LHCP incident wave through both components, while RHCP waves are reflected.

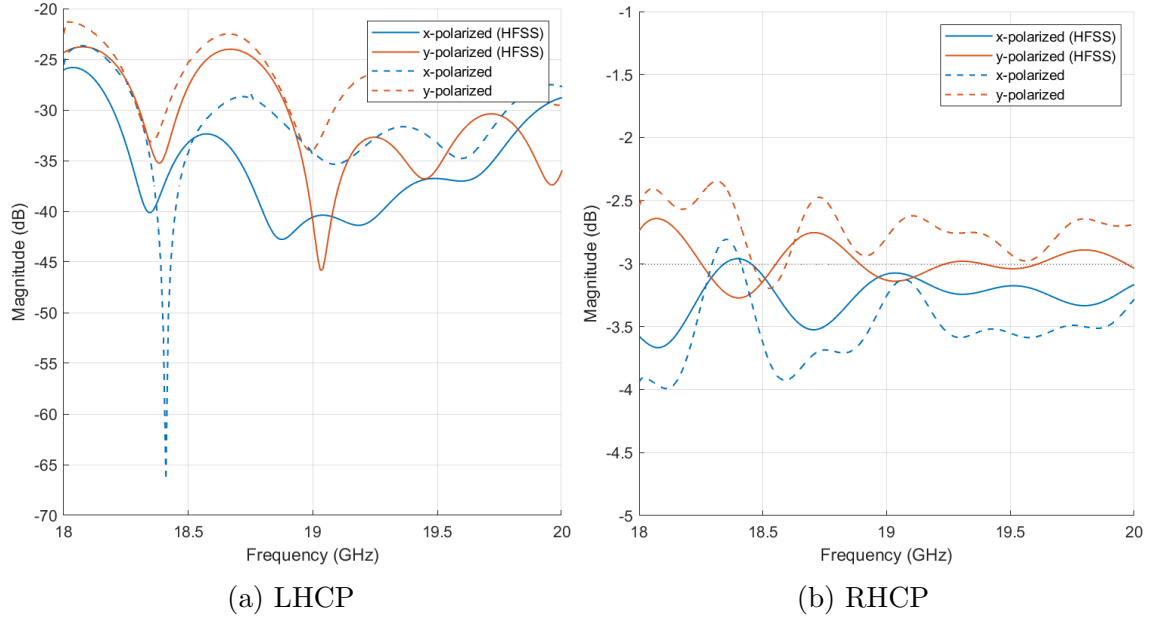


Figure 3.6: S_{11} of LHCP and RHCP wave through both components in series. HFSS simulation in solid lines, T parameter equivalent in dashed lines

The results match the qualitative prediction. LHCP waves have low reflection, with Active S_{11} \approx -20 dB (Fig. 3.6a), and high transmission into the propagating TE_{10} mode in the rectangular waveguide, with Active S_{21} of nearly 0 dB (Fig. 3.7a). RHCP waves, by contrast, reflect with half of the incident power (-3 dB) into the x- and y-polarized modes (Fig. 3.6b), and have low transmission into the propagating mode with Active S_{21} \approx -20 dB.

The T parameter calculations based on each component simulated independently (dotted lines in Figs. 3.6 and 3.7) reproduce the order of magnitude and general trend of the actual HFSS simulation of both components in series, though fine features of the plots are not shared. Differences between the simulation and calculation are likely attributable to differences in how the two components are meshed in the finite element analysis setup. Despite these differences, a qualitative comparison of the two validates the use of the 4-port T parameter method for simulating components in series, which may be leveraged to save the time of performing expensive multi-component simulations with a prohibitively large mesh.

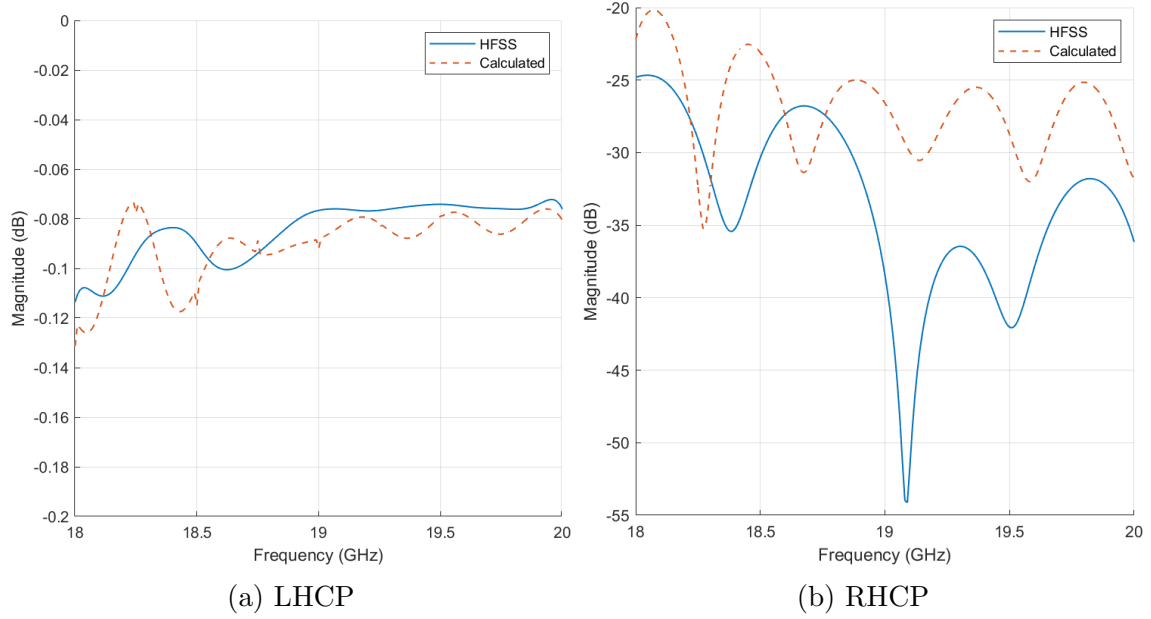


Figure 3.7: S_{21} of LHCP and RHCP wave through both components in series. HFSS simulation in solid lines, T parameter equivalent in dashed lines

3.2 Constructing a simulated CRES source

Expressions for the near-field electric and magnetic fields of a CRES source were generated on the surface of a 3mm cube source geometry (2.4) over a frequency range of 18 to 19 GHz in 20 MHz intervals. These were assigned to a source cube of the same dimensions in HFSS, modeled inside a 0.455" diameter circular waveguide. The electric field of CRES radiation simulated at 18 GHz along the center line of the waveguide is plotted in Figure 3.8.

The circular polarization of the radiation is evident by inspection, though there is some small distortion to the rotation of the E-field vector as it propagates.

3.2.1 Simulated CRES source power spectrum

We measured the power outputted by the simulated CRES source by calculating the Poynting flux at both ends of the decay cell following a polarizer and transition to a rectangular waveguide.

The nonlinear total power, which oscillates between 18.5 and 25 fW, is not a desirable result, and may suggest an issue with the simulated CRES source. Additionally, almost no power is delivered to port 1 around 18.25 GHz, and almost all the power from the source is delivered to side 2 around this frequency. Either this is an issue with the directionality of radiation from the source, or radiation at this frequency radiated towards port 1 is improperly circularly polarized, reflecting off the polarizer and waveguide transition and transmitting into port 2 instead.

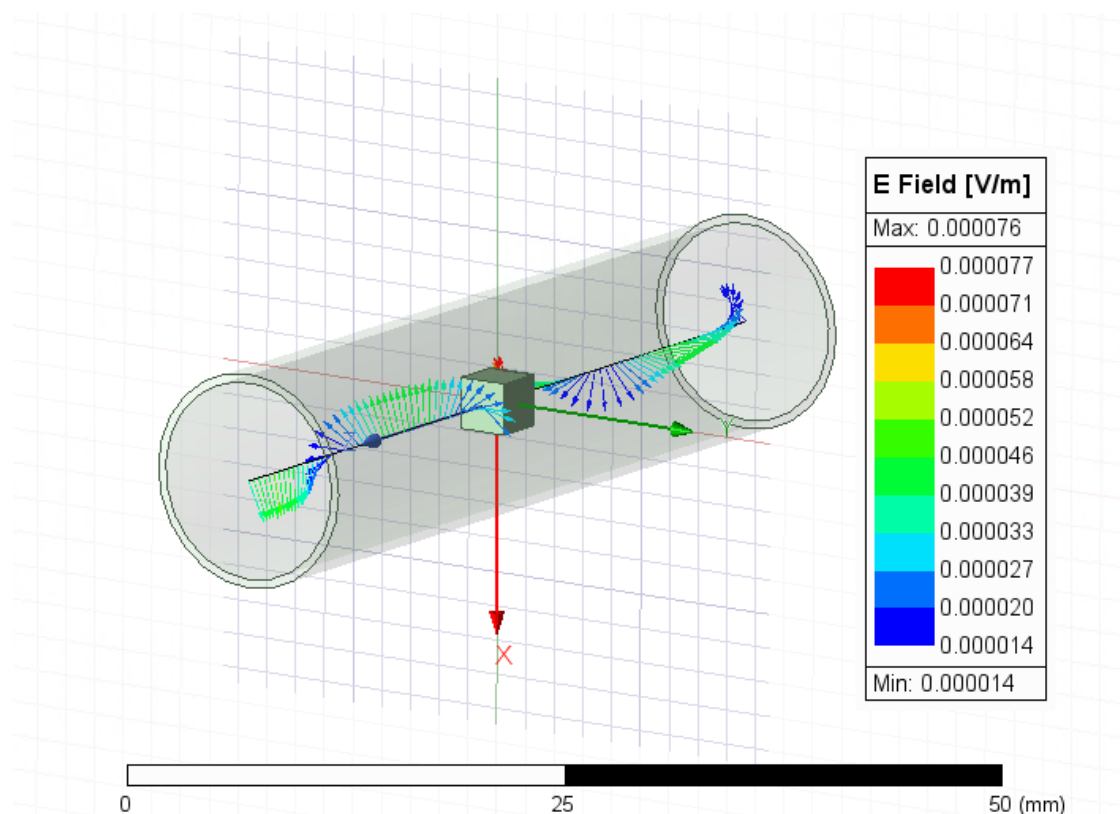


Figure 3.8: E-field radiated from a simulated CRES source with cube source geometry at 18 GHz

3.3 Power delivered to LNA

The CRES fields were simulated over a frequency range of 18 GHz to 19 GHz, with 20 MHz frequency resolution. The Poynting flux through the waveguide cross section at the location of the LNA readout was calculated at 20 MHz intervals and is plotted below. The system was simulated with fully reflective waveguide termination, a realistic termination, and an ideal termination.

With a reflective termination in place, the power delivered to the LNA output exhibits large amplitude oscillations across the frequency range (Figure 3.10). When using a realistic termination model with $S_{11} \approx -6$ dB, the oscillations remain present but have a greatly reduced amplitude (Figure 3.11). The oscillations are spaced by about 80 MHz, slightly lower than the 90 MHz spacing in data, meaning the modeled distance between the CRES source and terminator might be slightly larger than the real distance. With the perfect termination, the main oscillations disappear, but there is still a large decrease in power at around 18.3 GHz and a peak around 18.7 GHz. This is possibly due to the non-uniform power from the CRES source towards port 1 of the decay cell in Figure 3.9.

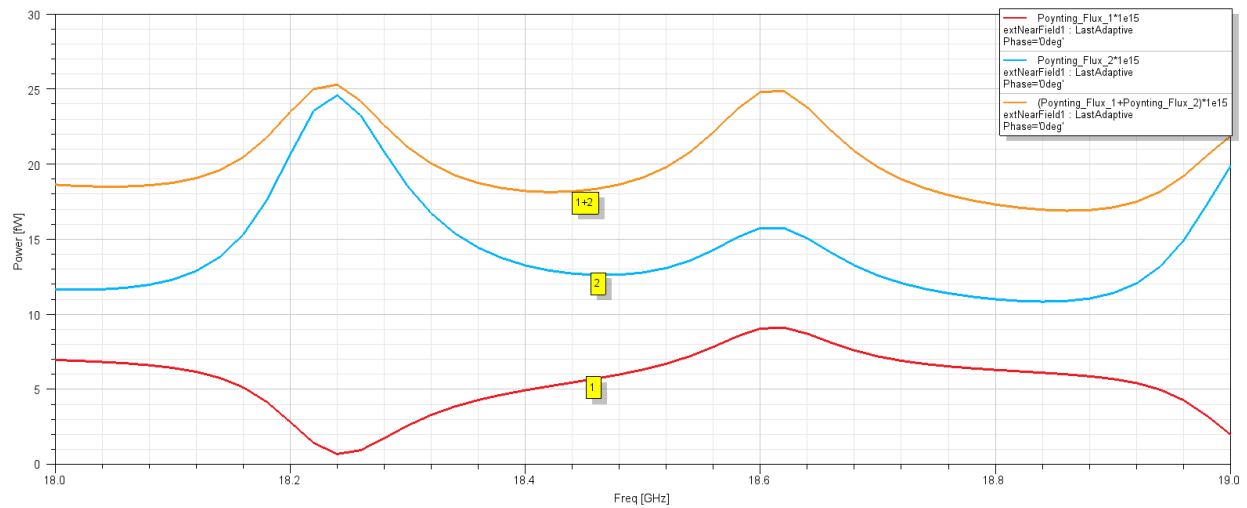


Figure 3.9: Power spectrum of the CRES source delivered to the rectangular waveguides in either direction (red: port 1, blue: port 2) and total power (orange)

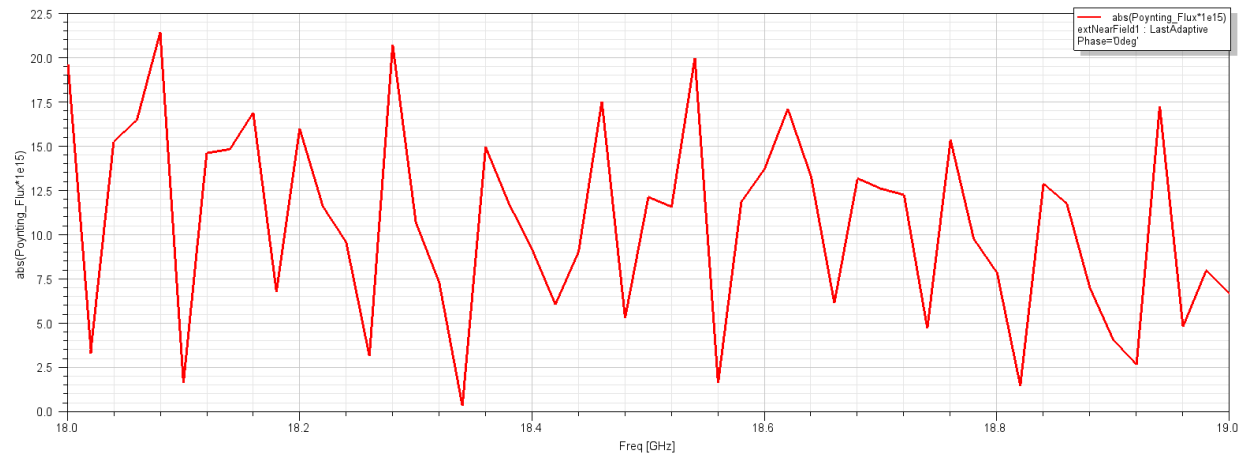


Figure 3.10: Power flow in the rectangular waveguide waveguide [fW] at LNA from 18 to 19 GHz with a reflective waveguide termination.

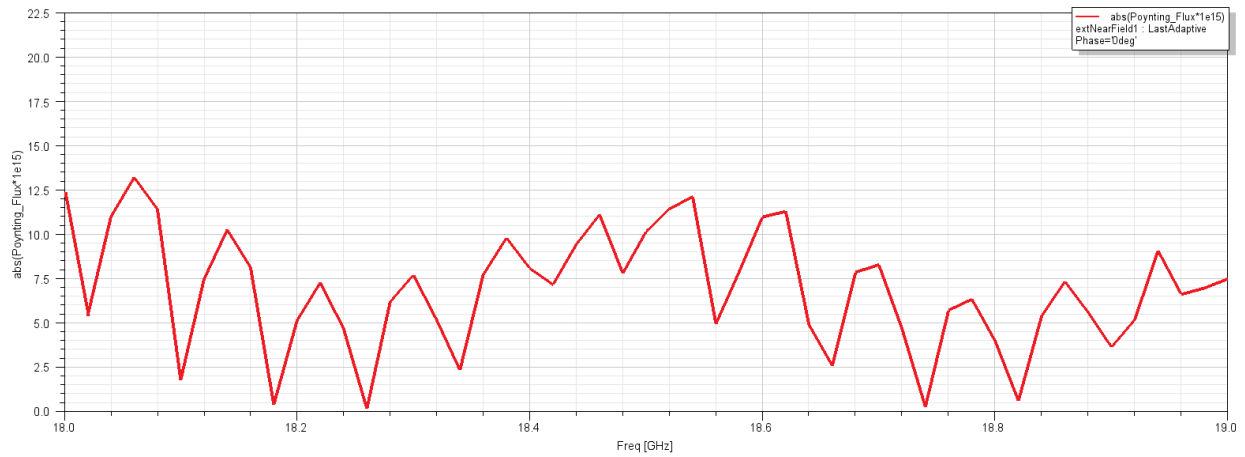


Figure 3.11: Power flow in the rectangular waveguide [fW] at LNA from 18 to 19 GHz with a realistic waveguide termination.

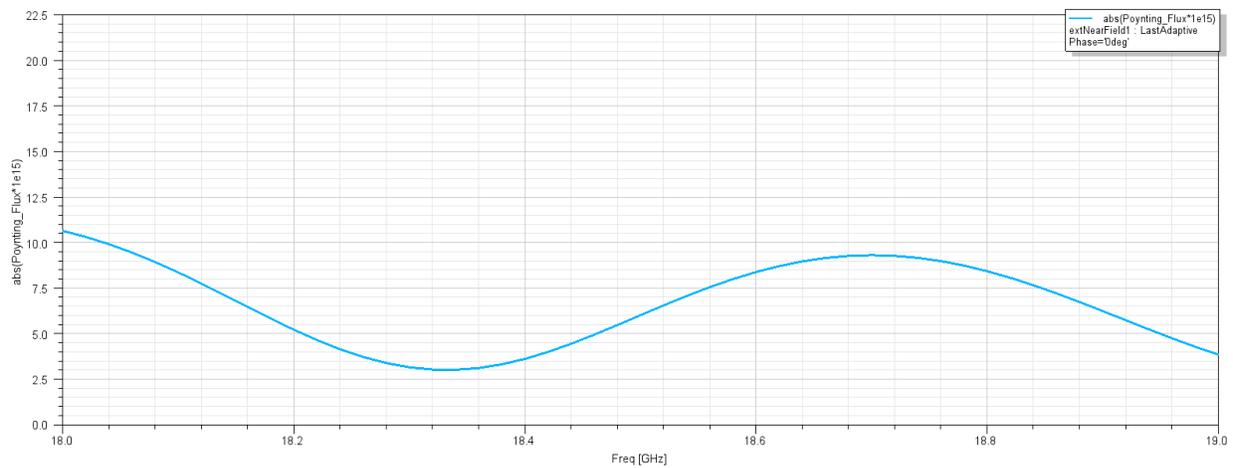


Figure 3.12: Power flow in the rectangular waveguide [fW] at LNA from 18 to 19 GHz with a perfect waveguide termination.

Chapter 4

Discussion

4.1 Summary

In this work, I present a CAD model and numerical simulations of the He6-CRES waveguide system in Ansys HFSS. These simulations were developed to characterize frequency variations in the signal-to-noise ratio due to interference effects in the waveguide, a major source of systematic error in taking broadband CRES data. Access to a fully parametric electromagnetic simulation of the waveguide system allows the group to quickly and inexpensively model the effect of any hardware upgrade or modification, or to inform relevant design choices before making hardware purchases and installation.

Interference effects are caused by reflections off of waveguide components, so I began by simulating the S-parameters of key components the quarter-wave polarizer, the circular-to-rectangular waveguide transition, and the waveguide termination. Since the fundamental mode in a circular waveguide is axially symmetric, it can be decomposed into two degenerate orthogonal polarizations along x and y, which are treated as independent ports for S-parameter solutions in Ansys HFSS. The S-parameters of the polarizer showed very little incident power reflected for a linearly or circularly polarized incident wave. Furthermore, the relative phase shift between x and y polarizations transmitting through the polarizer was within $90^\circ \pm 1^\circ$ and the axial ratio was below 0.04 dB, indicating nearly perfect quarter wave polarization over the frequency range of interest. The waveguide transition from a circular waveguide to a WR42 rectangular waveguide completely reflects an incident x-polarized mode, which is orthogonal to the polarization of the fundamental mode, but it transmits the y-polarized mode with very low loss. A circularly polarized wave incident on the waveguide transition transmits and reflects half of the incident power: the wave can be decomposed into fully transmitted and fully reflected components which are orthogonal with equal amplitude. The waveguide termination was simulated to have an S_{11} on the order of -10 dB, falling an order of magnitude short of the desired -20 dB or better design specification. This figure should be compared to experimental measurements of the terminator S_{11} to verify if the epoxy-graphite blended material used to cast the terminator is being properly simulated in HFSS.

I then modeled the full He6-CRES waveguide system including the CRES decay cell, including a simulated source of CRES radiation. The source was created by assigning electric

and magnetic fields to the surface of a 3mm cube source geometry as an incident wave. The fields were calculated numerically at solution frequencies in 20 MHz increments from 18 to 19 GHz from an analytic solution for the Liénard–Wiechert potentials of an on-axis β particles undergoing cyclotron motion in a circular waveguide. Successfully importing the fields seems to be dependent on the order in which the points on the source lattice are indexed or spatially arranged: a successful configuration was achieved for a cubic source by trial-and-error, but I did not succeed in generating a functional cylindrical source geometry for this project. The cubic source geometry may contribute to a non-uniform total power spectrum radiating from the source, and other potential non-idealities which remain to be identified and rectified.

The signal delivered from the CRES source to the LNA was calculated as the Poynting flux through the waveguide cross section at the location where an RF circulator couples the waveguide to low-noise amplifiers in the physical experiment. The numerical surface integral was optimized to a much quicker single variable integral: in principle, the delivered power could be calculated from just the z-component of the Poynting vector at the center of the rectangular waveguide, since only the TE_{10} mode propagates. I varied the terminator reflectivity between an ideal termination, a realistic termination, and a fully reflective termination. The simulations with non-ideal terminations produced oscillations in signal amplitude at the other end of the waveguide with similar peak spacing to the experimental SNR oscillation data. The realistic, less reflective termination had a smaller oscillation amplitude than the fully reflective termination. The ideal termination did not produce the closely spaced oscillations, but did have a much wider oscillation that is either a product of a much shorter path length reflection in the system or simply an artifact of the non-uniform simulated CRES source.

4.2 Outlook

He6-CRES aims to measure the Fierz interference term b_{Fierz} to a sensitivity of 10^{-3} from the beta decays of ${}^6\text{He}$ and ${}^{19}\text{Ne}$ using Cyclotron Radiation Emission Spectroscopy. The experiment is currently being prepared for a data-taking run targeting 10^{-2} sensitivity which will address major sources of uncertainty before working to correct other sources of error to achieve the target sensitivity to search for physics Beyond the Standard Model.

In the long term, He6-CRES will serve not just as a new precision measurement of b_{Fierz} , but also as a demonstration of the applicability of CRES towards broadband beta spectroscopy in general. As compared to Project 8, which only takes measurements in a small energy range around the tritium beta spectrum endpoint, He6-CRES uses both a broad data collection bandwidth and a varying magnetic field to cover the entire energy range of nuclear decays. Achieving the target measurement sensitivity would establish CRES as a tool to be used in nuclear physics laboratories for any of a wide range of experiments requiring beta spectroscopy: for example as a new instrument at the Facility for Rare Ion Beams (FRIB).

Bibliography

- [1] W. Byron et al. “First Observation of Cyclotron Radiation from MeV-Scale e^\pm following Nuclear β Decay”. In: *Phys. Rev. Lett.* 131 (8 Aug. 2023), p. 082502. DOI: 10.1103/PhysRevLett.131.082502. URL: <https://link.aps.org/doi/10.1103/PhysRevLett.131.082502>.
- [2] H. Saul et al. “Limit on the Fierz Interference Term b from a Measurement of the Beta Asymmetry in Neutron Decay”. In: *Phys. Rev. Lett.* 125 (11 Sept. 2020), p. 112501. DOI: 10.1103/PhysRevLett.125.112501. URL: <https://link.aps.org/doi/10.1103/PhysRevLett.125.112501>.
- [3] Vincenzo Cirigliano et al. *Precision Beta Decay as a Probe of New Physics*. 2019. arXiv: 1907.02164 [nucl-ex].
- [4] W. Pauli. *Dear radioactive ladies and gentlemen*. Note: Open letter to the group of radioactive people at the Gauverein meeting in Tübingen in 1930. A translation from German to English appeared in the article “The idea of the neutrino” Laurie M. Brown, *Phys.Today* 31N9 (1978) 23-28 [DOI: 10.1063/1.2995181]. Dec. 1930.
- [5] C. S. Wu et al. “Experimental Test of Parity Conservation in Beta Decay”. In: *Phys. Rev.* 105 (4 Feb. 1957), pp. 1413–1415. DOI: 10.1103/PhysRev.105.1413. URL: <https://link.aps.org/doi/10.1103/PhysRev.105.1413>.
- [6] Tanmoy Bhattacharya et al. “Probing novel scalar and tensor interactions from (ultra)cold neutrons to the LHC”. In: *Phys. Rev. D* 85 (5 Mar. 2012), p. 054512. DOI: 10.1103/PhysRevD.85.054512. URL: <https://link.aps.org/doi/10.1103/PhysRevD.85.054512>.
- [7] Vincenzo Cirigliano, Susan Gardner, and Barry R. Holstein. “Beta decays and non-standard interactions in the LHC era”. In: *Progress in Particle and Nuclear Physics* 71 (July 2013), pp. 93–118.
- [8] Ayala Glick-Magid et al. “Nuclear *ab initio* calculations of ${}^6\text{He}$ β -decay for beyond the Standard Model studies”. In: *Physics Letters B* 832 (Sept. 2022), p. 137259. ISSN: 0370-2693. DOI: 10.1016/j.physletb.2022.137259. URL: <https://www.sciencedirect.com/science/article/pii/S0370269322003938> (visited on 04/22/2024).
- [9] Fry, J. et al. “The Nab experiment: A precision measurement of unpolarized neutron beta decay”. In: *EPJ Web Conf.* 219 (2019), p. 04002. DOI: 10.1051/epjconf/201921904002. URL: <https://doi.org/10.1051/epjconf/201921904002>.

- [10] Benjamin Monreal and Joseph A. Formaggio. “Relativistic cyclotron radiation detection of tritium decay electrons as a new technique for measuring the neutrino mass”. In: *Phys. Rev. D* 80 (5 Sept. 2009), p. 051301. DOI: 10.1103/PhysRevD.80.051301. URL: <https://link.aps.org/doi/10.1103/PhysRevD.80.051301>.
- [11] D. M. Asner et al. “Single-Electron Detection and Spectroscopy via Relativistic Cyclotron Radiation”. In: *Phys. Rev. Lett.* 114 (16 Apr. 2015), p. 162501. DOI: 10.1103/PhysRevLett.114.162501. URL: <https://link.aps.org/doi/10.1103/PhysRevLett.114.162501>.
- [12] Ch. Weinheimer. “KATRIN, a next generation tritium β decay experiment in search for the absolute neutrino mass scale”. In: *Progress in Particle and Nuclear Physics* 48.1 (Jan. 2002), pp. 141–150. ISSN: 0146-6410. DOI: 10.1016/S0146-6410(02)00120-5. URL: <https://www.sciencedirect.com/science/article/pii/S0146641002001205> (visited on 09/11/2023).
- [13] J.D. Jackson. *Classical Electrodynamics*. 3rd ed. John Wiley & Sons, 1999.
- [14] David M. Pozar. *Microwave Engineering*. 4th ed. Hoboken, NJ: Wiley, 2012. ISBN: 978-0-470-63155-3.
- [15] C. A. Balanis. *Advanced Engineering Electromagnetics*. 2nd. Hoboken, NJ: John Wiley & Sons, Inc., 2012.
- [16] R. E. Collin. *Field Theory of Guided Waves*. 2nd. New York, NY: John Wiley & Sons, Inc., 1990.
- [17] N. Buzinsky et al. *Larmor Power Limit for Cyclotron Radiation of Relativistic Particles in a Waveguide*. 2024. In preparation.
- [18] James Frei, Xiao-Ding Cai, and Stephen Muller. “Multiport S -Parameter and T -Parameter Conversion With Symmetry Extension”. In: *IEEE Transactions on Microwave Theory and Techniques* 56.11 (Nov. 2008), pp. 2493–2504. ISSN: 1557-9670. DOI: 10.1109/TMTT.2008.2005873.
- [19] T. Reveyrand. “Multiport conversions between S, Z, Y, h, ABCD, and T parameters”. In: *2018 International Workshop on Integrated Nonlinear Microwave and Millimetre-wave Circuits (INMMIC)*. Brive La Gaillarde: IEEE, July 2018. ISBN: 978-1-5386-5507-8. DOI: 10.1109/INMMIC.2018.8430023. URL: <https://ieeexplore.ieee.org/document/8430023/> (visited on 08/06/2023).
- [20] Ansys product website. URL: <https://www.ansys.com/products/electronics/ansys-hfss>.
- [21] Luciano Malavasi. *Modeling a Quarter Wave Plate in a Circular Waveguide with Ansys HFSS*. (Internal Report). July 2023.
- [22] Raphael Cervantes. *The Project 8 Phase IIb Terminator*. (Internal Report). Aug. 2018.

Appendix A

Noise

The results presented in this report only concern oscillations in signal amplitude. Equally important to reconstructing the SNR oscillations in simulation is a comprehensive noise analysis. Decoherent thermal noise originates from every where in the waveguide system. Ansys HFSS does not natively include tools to perform analysis of thermal noise originating from waveguide components. This work does not extensively investigate the power spectrum of incoherent noise inside the He6-CRES waveguide system.

Until a more robust noise model is constructed, we make the simplifying assumption that the LNA readout is the dominant noise source in the system, and approximate the noise spectrum by considering the S_{11} at the output port. This plot is presented below for the realistic and fully reflective terminations.

Even from this simplified model, we observe that the peak noise is 5 dB worse without the epoxy termination in place. The maximum values of the S_{11} oscillations are about -10 dB with a fully reflective termination, and vary between -15 dB and -20 dB with the realistic termination model. We hope that a further improved waveguide termination might further reduce the noise amplitude by -5 to -10 dB.

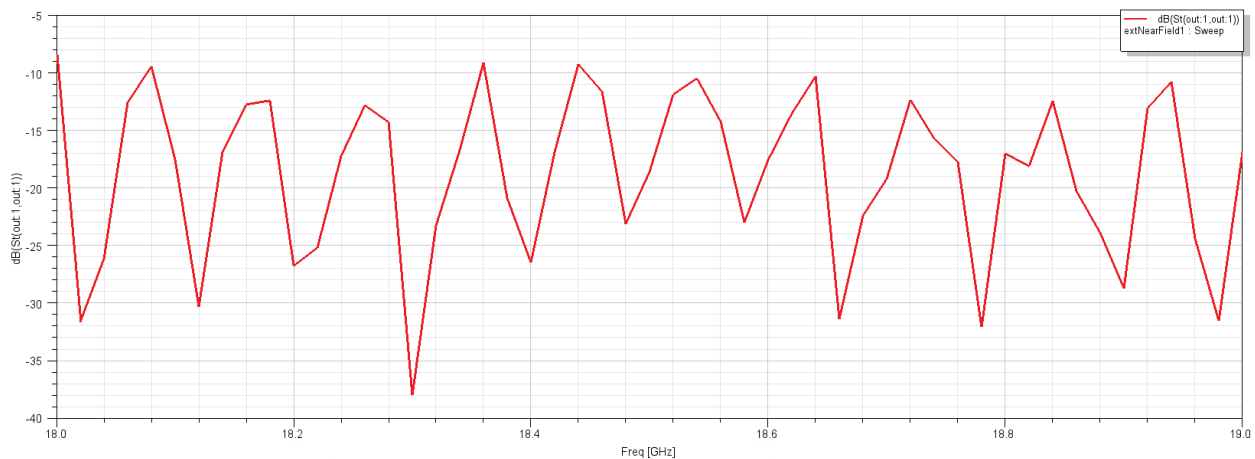
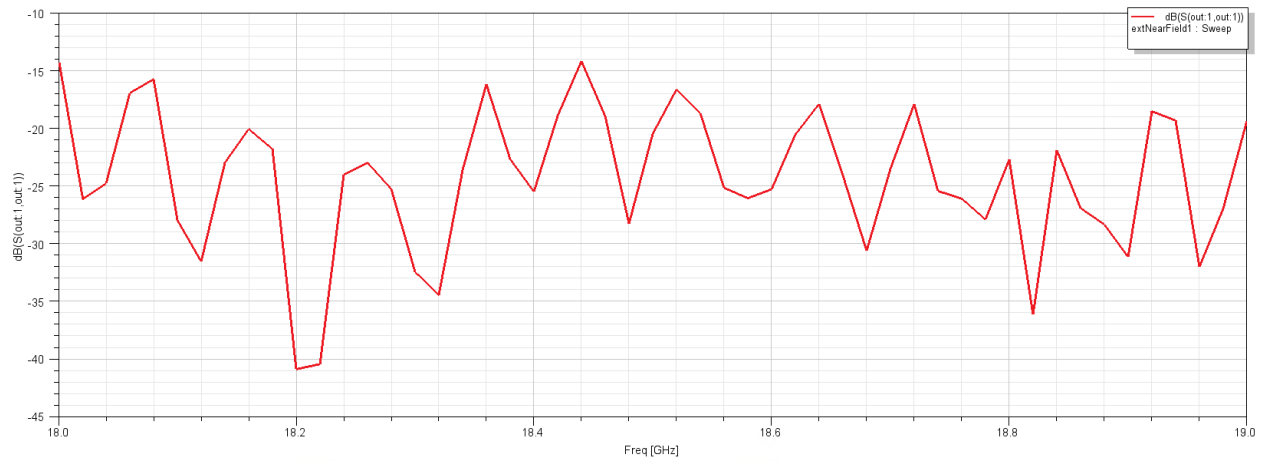


Figure A.1: S_{11} at output port with a fully reflective termination

Figure A.2: S_{11} at output port with realistic termination